*Article*

# Analysis of Internal Solitary Waves in the Gulf of Oman and Sources Responsible for Their Generation

**Kamran Koohestani [1],\*, Yury Stepanyants [2,3] and Mohammad Nabi Allahdadi [4]**

[1] School of Civil Engineering, University of Tehran, Tehran 1417853111, Iran
[2] School of Mathematics, Physics and Computing, University of Southern Queensland, Toowoomba, QLD 4350, Australia
[3] Department of Applied Mathematics, Nizhny Novgorod State Technical University n.a. R.E. Alekseev, 603950 Nizhny Novgorod, Russia
[4] Department of Marine, Earth and Atmospheric Sciences, North Carolina State University, Raleigh, NC 27607, USA
\* Correspondence: koohestani@ut.ac.ir

**Abstract:** A combination of multiple data sources has been used to study the characteristics of internal solitary waves (ISWs) in the Gulf of Oman (GoO). Water column stratification in the Gulf has been examined using field observations and World Ocean Atlas 2018 datasets. The spatiotemporal distribution of ISWs has been obtained from satellite images obtained by means of Synthetic Aperture Radar (SAR) and optical sensors taken from 2018 to 2020. The mechanisms of ISW generation in the GoO have been studied using the data revealed from different available sources. The results show that there are annually two major typical stratifications in the GoO throughout the year, strong stratification in May through September and weak stratification during other months. Dispersion relations corresponding to these types of stratification have been obtained with acceptable accuracy for both deep and shallow regions. The spatiotemporal distribution of ISWs demonstrates that the western and southern regions of the GoO are the hotspots for generation of ISWs in this basin. Several mechanisms of ISW generation in the GoO are discussed including tide, eddies, lee waves, and atmospheric perturbation; the latter one is, apparently, responsible for the appearance of large-amplitude ISWs.

**Keywords:** Gulf of Oman; internal solitary waves; SAR; optical image; mechanisms of internal wave generation

## 1. Introduction

Internal solitary waves (ISWs) attract the interest of many researchers as they play an important role in oceanic processes such as the transport of mass, momentum, nutrients, heat, and sediment. They also contribute to the mixing processes and onset of turbulence. Great progress has been achieved in past decades in the theoretical and numerical studies of internal waves; new computational models have been developed to allow researchers to simulate oceanic processes using the primitive set of hydrodynamic equations. In the meantime, the number of field expeditions has been reduced in comparison with 1970–1980 when many countries conducted instrumental measurements of internal waves and other oceanic processes in different areas of the world ocean. In such a situation, great value acquires the study of internal waves through satellite observations and analysis of images taken from aircraft and obtained by means of Synthetic Aperture Radars (SAR) and optical instruments. Nowadays there is a vast number of publications reporting of ISWs detections in various basins all over the globe, see, for example, [1–11]. The results obtained from the data processing are basically in good agreement with the theoretical models including the rather simplified Korteweg–de Vries (KdV) model.

A few studies have been also carried out on the ISWs in the Gulf of Oman (GoO) majorly using numerical models and field observations (see the references below). The GoO is a basin with one of the most intense ship traffic in the world. This makes the study of internal wave dynamics in this region imperative. Small and Martin, using two SAR images detected nonlinear internal waves generated by a tide in the GoO [12]. They also developed a numerical model to evaluate the tidal currents and the mechanism of wave generation in a spring tide which supported their interpretation of satellite images. Moreover, their numerical study revealed that similar ISWs can be generated in other times throughout the year if the thickness of the near-surface layer containing less dense water is sufficiently small (about 10 m). Other researchers deployed field measurements and numerical analysis to study ISWs in the GoO (see [13] and references therein). Tide is known as the most common driving force of ISW generation in the ocean, although, several other mechanisms can also contribute in generation of internal waves. One of them is the well-known mechanism of generating ISWs by the interaction of strong flows with underwater sills leading to the generation of so-called lee waves. A number of studies distinguish this mechanism using theoretical, numerical, and observational measurements [14].

Unlike the mentioned two mechanisms, there are other driving mechanisms in which details of their progress have remained obscure. Atmospheric perturbations, including wind and pressure fields, are the important exciting mechanisms that are believed to generate ISWs in the ocean. As foratmospheric pressure, a majority of theoretical studies have considered the resonant effects of pressure fields through which the energy is transferred from the atmosphere to the oceanic thermocline. Leonov and Miropolsky introduced a more general model in which the characteristics of generated ISWs are determined by the atmospheric pressure spectrum [15]. Studies showed that an atmospheric pressure field traveling at a low speed can generate internal waves like a moving vessel but on a much larger scale [16]. Several studies have been also performed to describe wind-driven IWs. Through these studies, it has been demonstrated that the divergence and convergence of wind velocity, as well as time-space varying wind fields, can excite baroclinic instabilities [16–18].

Another mechanism whose details have not been well-understood yet despite theoretical attempts is generation by ocean eddies. In several studies, the generation of IW fields by mesoscale and sub-mesoscale eddies was evaluated using theoretical,numerical, and observational approaches. Internal waves can be directly produced by eddies or indirectly through various phenomena associated with eddies including drained energy, eddy-topography interaction, breaking of eddies, etc. The earliest report of the coexistence of internal waves with mesoscale eddies as observed by SAR images was presented by Fu and Holt but the authors did not relate IWs to the eddies [19]. Such waves were then observed in SAR images and pointed out by other researchers [20,21]. Additionally, Sandven and Johannessen, and Johannessen et al. presented a SAR image showing a small eddy with the characteristic scale of 5 km where IWs with wavelengths of a few hundred meters up to 1000 m were radiating out of the center of the eddy [22,23]. This mechanism can be substantially important in the GoO owing to the well-documented persistent existence of mesoscale and sub-mesoscale eddies in this basin [24,25].

It has been also demonstrated that, under specific hydraulic conditions, the interaction of a strong flow with a Kelvin wave enhances the progress through which IWs are generated [26]. Because of Kelvin waves, originating from the Arabian Sea and occasionally entering the GoO , this mechanism can play an important role in certain regions of the GoO where favorable hydraulic conditions are satisfied (e.g., east of the Strait of Hormuz) [27–29]. More descriptions and references on the mechanisms of IWs generation can be found in [30].

In this paper, we focus on the main mechanisms of internal wave generation in the GoO. Precise determining of ISW characteristics usually needs field measurements that are expensive. Besides, such measurements enable us to examine only limited cases that

occur at certain places and at a certain time of observation. Hence, it would be extremely usefulto use freely available global datasets for studying ISWs with an acceptable accuracy over the entire basin. The primary goal of this study is to pinpoint the spatiotemporal distribution of ISWs in the GoO, reveal mechanisms of their generation, and determine the characteristics of such waves. To this end, we use satellite images of ISWs from January 2018 to November 2020, as well as SAR and optical images. The data obtained from the analysis of images are utilized in conjunction with other sources of physical, hydrological, and atmospheric datasets. The results then serve as information to infer the characteristics of ISWs using theoretical models.

The paper is organized as follows. In Section 2 we describe the study area, present data on wind and atmospheric pressure in the GoO, the utilized datasets, and the theoretical models widely used for the description of long internal waves in the oceans. In Section 3 we present the results of our analysis including spatiotemporal distributions and characteristics of ISWs in the GoO. In Section 4 the results obtained are discussed and the mechanisms of ISW generation in the GoO are evaluated. Furthermore, a general zonation regarding the activity and driving forces of ISWs in the GoO is suggested. Lastly, in the conclusion, we summarize the results and discuss perspectives of further studies of ISW in the GoO.

## 2. Study Areaand Theoretical Models

### 2.1. Study Area

The study area encompasses the GoO which joins the Persian Gulf (PG) in the west through the Strait of Hormuz to the Arabian Sea (AS) in the east (see Figure 1). Therefore, the oceanography and hydrodynamics of the study area is affected by both PG and AS. The length of the GoO basin is about 560 km and the width changes from roughly 50 km at the Strait of Hormuz to 320 km in the eastern mouth in the vicinity of the AS. The depth in the GoO varies significantly from 100 meters and less on the shelves to about 3500 m in the deepest parts. GoO represents a transient zone between the PG as an extremely saline marginal sea and oceanic water in the AS. PG water experiences an initial mixing in the GoO prior to entering the AS. A number of oceanographic phenomena (such as tidal currents, mesoscale and sub-mesoscale eddies, Kelvin waves, etc.) occur in this limited semi-closed basin resulting in intricate hydrodynamics. Despite the important role of ISWs in water mixing in this region, only a few studies have been carried out thus far on this issue.
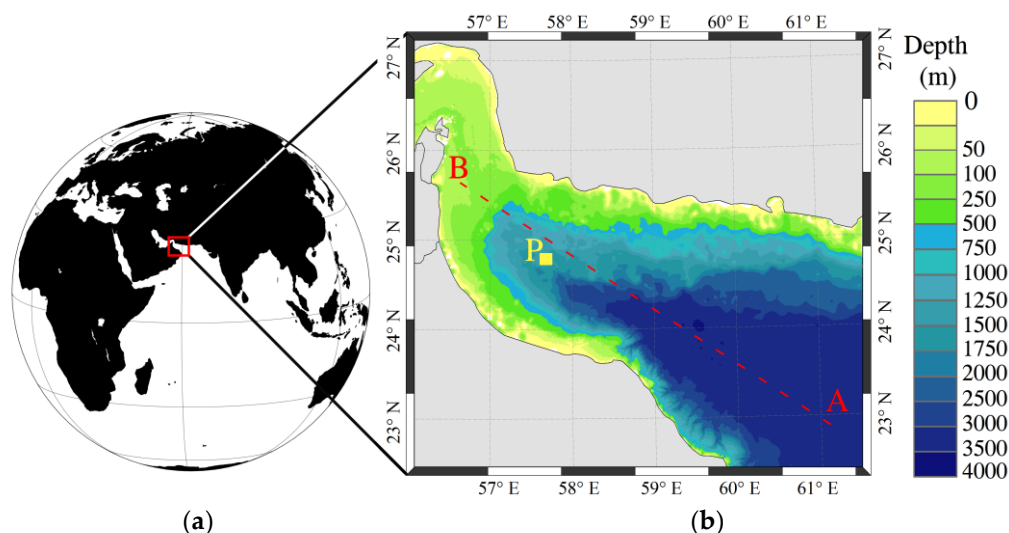


**Figure 1.** Location (**a**) and bathymetry (**b**) of the Gulf of Oman. Dashed line AB shows the cross-section along which water stratification will be shown in Figure 2.
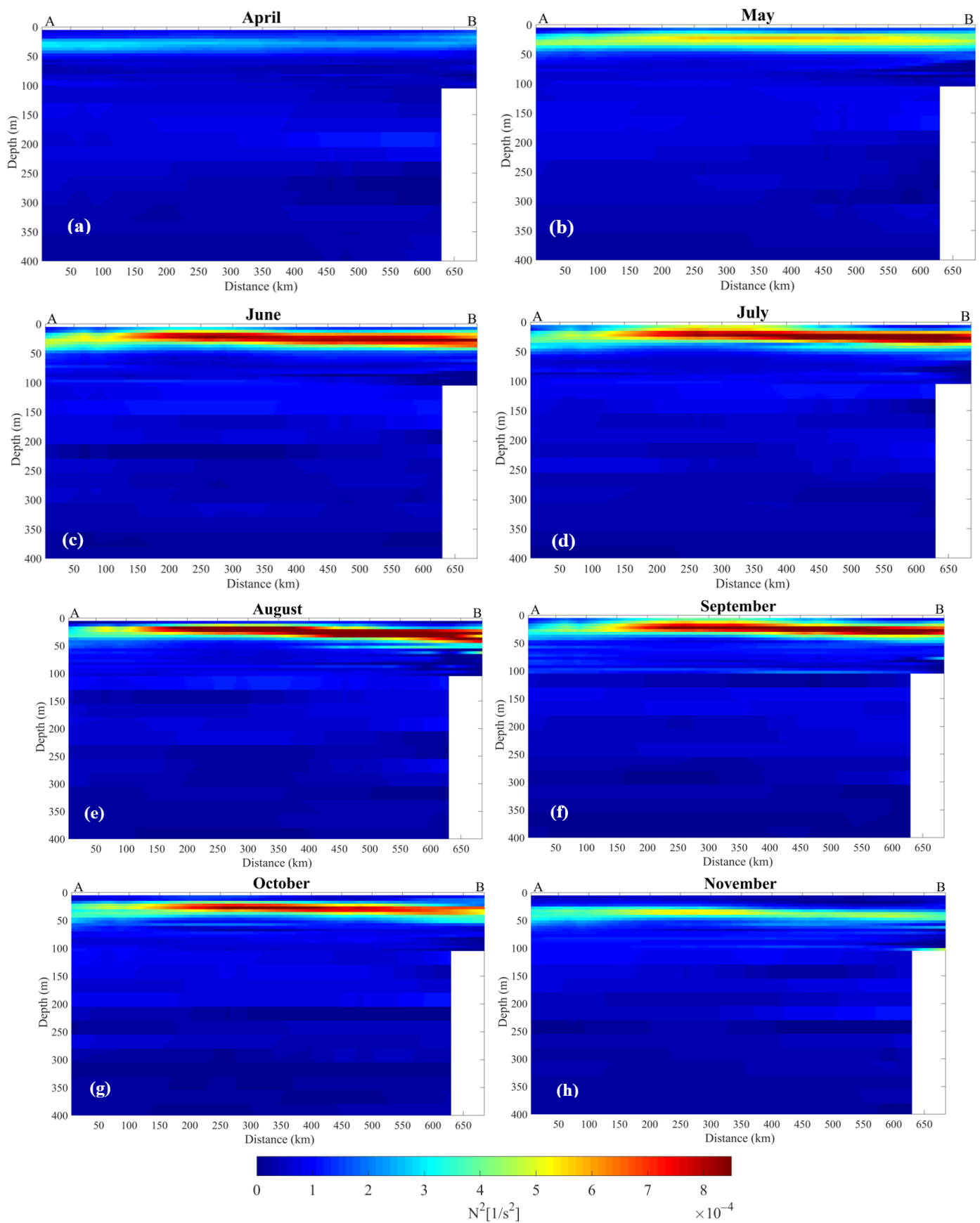
**Figure 2.** Vertical profiles of Brunt–Väisälä squared frequency, $N^2$ [1/s²], from April (**a**) to November (**h**) along the AB line shown in Figure 1. In each figure, as labeled, the points A and B on line AB are located on the left and right side of the plot, respectively.

In the meantime, the GoO is rarely affected by extreme events such as cyclones which can drastically change the stratification [25,31] and, therefore, a distinct seasonally stratification exists in this basin. Nevertheless, there are some factors that may regionally modify the depth of the thermocline, solely or by their interactions, including mesoscale and submesoscale eddies, upwelling, and intrusion of PG water. However, as will be demonstrated, long time-averaged data can properly represent the stratification in the GoO providing the results with reasonable accuracy.

### 2.2. World Ocean Atlas 2018

In this paper, we make use of the data on temperature and salinity profiles from the World Ocean Atlas (WOA 2018; [32]) in order to calculate monthly averaged characteristics of stratification in the GoO. The dataset has a horizontal resolution of 0.25 degrees and provides the temperature and salinity profiles in 57 depth levels from the surface down to 1500 m, distributed in 5-m intervals for the depth range from 0 m to 100 m, in 25-m intervals for the depth range from 100 m to 500 m, and in 50-m intervals for the depth range from 500 m to 1500 m.

### 2.3. Wind and Atmospheric Pressure

Wind and pressure fields are used to evaluate the forces generating ISWs. In this study, the fifth-generation ECMWF reanalysis (ERA5) [33] from the Copernicus program is utilized. This product has been derived from the full ERA5 dataset on the native resolution and regridded to a regular latitude–longitude grid of 0.25 degrees.

### 2.4. Theoretical Models Describing Long ISWs in the GoO

The stratification in the GoO in the spring–summer seasons is close to a two-layer system with a well-pronounced maximum of the Brunt–Väisälä frequency (it will be presented in the next section in Figure 2). Propagation of long nonlinear waves in a two-layer model of a finite depth ocean can be described by the Joseph–Kubota–Ko–Dobbs (JKKD) equation [34,35]:

$$\frac{\partial \eta}{\partial t} + c\frac{\partial \eta}{\partial x} + \alpha\eta\frac{\partial \eta}{\partial x} - \beta\frac{\partial^2}{\partial x^2}\wp\int_{-\infty}^{+\infty}\frac{\eta(x'/h_2,t)}{\tanh\left(\frac{\pi}{2}\frac{x-x'}{h_2}\right)}dx' = 0, \tag{1}$$

where $\eta(x, t)$ stands for the deviation of the interface between the layers from its equilibrium position, $h_1$ and $h_2$ are thicknesses of the upper and lower layers, respectively,

$$c = \sqrt{\frac{\Delta\rho}{\rho}g\frac{h_1 h_2}{h_1 + h_2}} \tag{2}$$

is the speed of long linear waves, $\Delta\rho$ is the density difference between the layers, $\rho$ is the average density of water, $g$ is the acceleration due to gravity, $\alpha = -3c/2h_1$ is the nonlinear coefficient, and $\beta = ch_1/4h_2$ is the dispersion coefficient; the symbol $\wp$ stands for the principal value of the integral. Here we use the Boussinesq approximation which formally corresponds to the limit when $\Delta\rho \to 0$, $g \to \infty$, but $\Delta\rho g$ = const.

Equation (1) reduces to the well-known KdV equation in the case when the characteristic wavelength $\Lambda$ of the interface perturbation is much greater than the thicknesses of both layers, $\Lambda \gg h_1, h_2$:

$$\frac{\partial \eta}{\partial t} + c\frac{\partial \eta}{\partial x} + \alpha_0\eta\frac{\partial \eta}{\partial x} + \beta_0\frac{\partial^3 \eta}{\partial x^3} = 0, \tag{3}$$

where $c$ is as above, and $\alpha_0 = \frac{3}{2}c\frac{h_1 - h_2}{h_1 h_2}$, $\beta_0 = \frac{ch_1 h_2}{6}$.

In another limiting case of infinitely deep ocean with a relatively shallow upper layer, the JKKD equation reduces to another popular model, the Benjamin–Ono (BO) equation:

$$\frac{\partial \eta}{\partial t} + c\frac{\partial \eta}{\partial x} + \alpha\eta\frac{\partial \eta}{\partial x} + \frac{\beta_1}{\pi}\frac{\partial^2}{\partial x^2}\wp\int_{-\infty}^{+\infty}\frac{\eta(x',t)}{x-x'}dx' = 0,\qquad(4)$$

where the coefficients are $c_1 = \sqrt{\Delta\rho g h_1/\rho}$, $\alpha$ is the same as in the JKKD equation, and $\beta_1 = ch_1/2$.

The dispersion relation for the JKKD equation is:

$$\omega = ck\left[1 - \frac{kh_1}{2\tanh(kh_2)}\right],\qquad(5)$$

where $k$ is the wavenumber and $\omega$ is the wave frequency. In the asymptotic limits when the JKKD equation reduces to the KdV and BO equations, the dispersion relation (5), becomes, respectively [34,35]:

$$\omega = ck - \beta_0 k^3 \qquad (kh_1 \ll 1; kh_2 \ll 1),\qquad(6)$$

$$\omega = c_1 k - \beta_1 k^2 \qquad (kh_1 \ll 1; kh_2 \gg 1).\qquad(7)$$

As one can see, the coefficients of these equations depend on the hydrological and physical properties of the basin. In order to understand the baroclinic properties of the GoO, the coefficients of the JKKD equation ($c$, $\alpha$, and $\beta$) were estimated throughout the basin using WOA climatological profiles. This provides a better understanding of the characteristics of internal waves in various parts of the GoO. Thus, depending on the characteristic width of a particular ISW and the local depth where the ISW is observed, the appropriate model, the KdV, JKKD, or BO can be used for the description of ISW propagation and evolution. An important remark should be made regarding the irregular geometry and bathymetry of the GoO and the non-constant location of the pycnocline across the water column. Such inhomogeneity of the basin leads to the necessity to augment the basic equation by the additional term which accounts for both the depth variation and variation of a pycnocline position. In this paper, we will not consider the long-term propagation of IWS, this will be conducted elsewhere later.

## 3. Results

### 3.1. Stratification in the GoO

Figure 2 illustrates the 2D profiles of squared Brunt–Väisälä frequency, $N^2$, in the GoO along the line AB shown in Figure 1. As one can see, the thermocline depth along the cross-section AB is notuniform; it sinks deeper in the western part of the basin compared to the middle part. The stratification commences forming in April and reaches its maximum strength in August. Then, it starts weakening until December and almost disappears in the winter period between December and March. It is noteworthy that according to observations, there are occasionally more than two layers in specific regions of the GoO mainly due to PG outflow. This can be observed in the western end of the profiles in Figure 2 from August to December. Khalilabadi et al. analyzed one-year oceanographic field measurements at the station located at 25° N and 57.5° E which showed a layer between 150–200 m depth generated by the PG outlet [36]. Sharp fluctuations in this layer were attributed to the IWs. These fluctuations were observed from May to August and were weaker in other months being stronger in spring and summer, weaker in autumn, and vanished in winter. This temporal pattern is compatible with the WOA profiles. The authors also showed that weaker density variations existed below 400 m with the same temporal behavior as in the upper layers. Using the Argo data, Khan et al. demon-

strated the existence of a patchy PG outlet in the GoO which emerged in the western part of GoO from March to November and attained a maximum stage in August [37].

In general, the individual and synergic effects of PG outlets and eddies can hypothetically play an important role in the formation of stratification in the GoO by producing more than two layers and changing the depth of the thermocline location. However, as mentioned, the existence of such effects is not detected at the time of ISW generation because PG outlet pathways and eddies are not permanent and change occasionally. As a water mass with an almost persistent flow pattern permanently enters the GoO with an almost constant annual cycle, it could be expected that intrusion of PG water is reflected in WOA which is a long-term averaged dataset. However, there is no change in Brunt–Väisälä frequency (see Figure 2) at the depths of the PG water pathway (200–300 m) [38]. This can be explained by the almost reciprocal compensation of two effects of the higher temperature and higher salinity. Therefore, there is no considerable density gradient produced as a result of the existence of PG water. However, this hypothesis is required an additional study using field measurements along the PGW pathway. Moreover, even if a strong stratification is produced by PG water, it is unlikely that perturbations in the upper layer can penetrate down to the usual depths of the PG outlet. As will be shown below, a two-layer model associated with WOA datasets makes a sufficiently accurate estimation of the characteristics of ISWs in the GoO.

Further studies would be essential using field observations and numerical models to evaluate the effects of PG outlet pathways and eddies and their temporal variations on the characteristics of ISWs in the GoO.

### 3.2. ISWs in the GoO: Spatiotemporal Distribution and Characteristics

Satellite, SAR, and optical images obtained from January 2018 to November 2020 were processed to study the spatiotemporal distributions of ISWs as well as their characteristics in the GoO. Figure 3 illustrates monthly spatial distributions of ISWs in the GoO identified during the study period; no ISWs were detected in January and December.
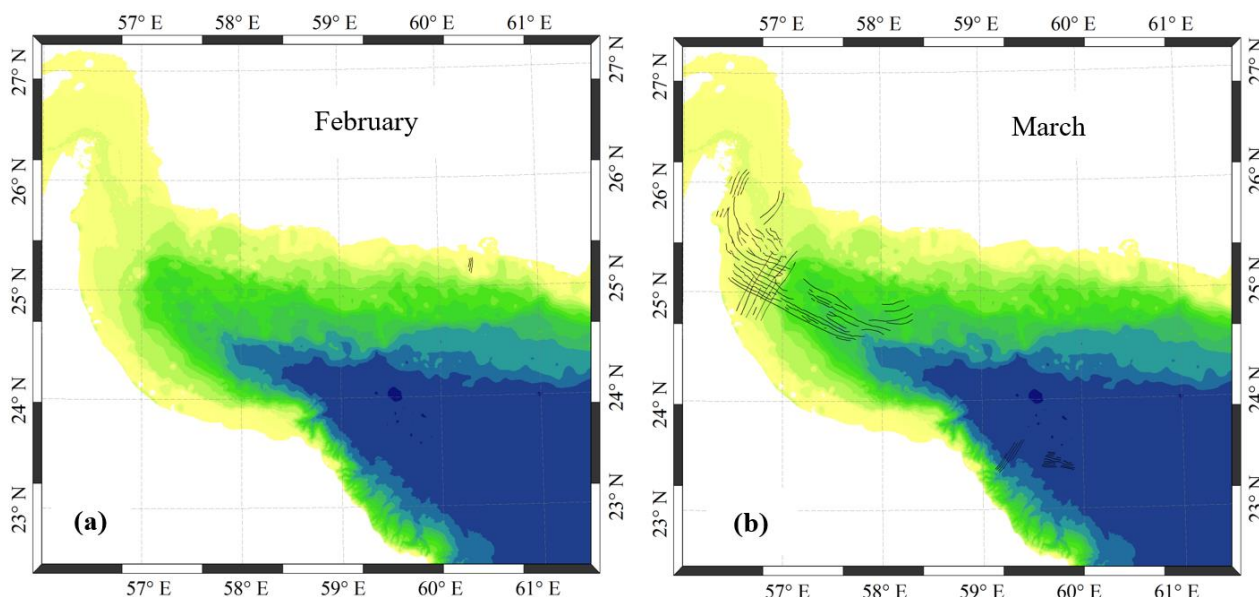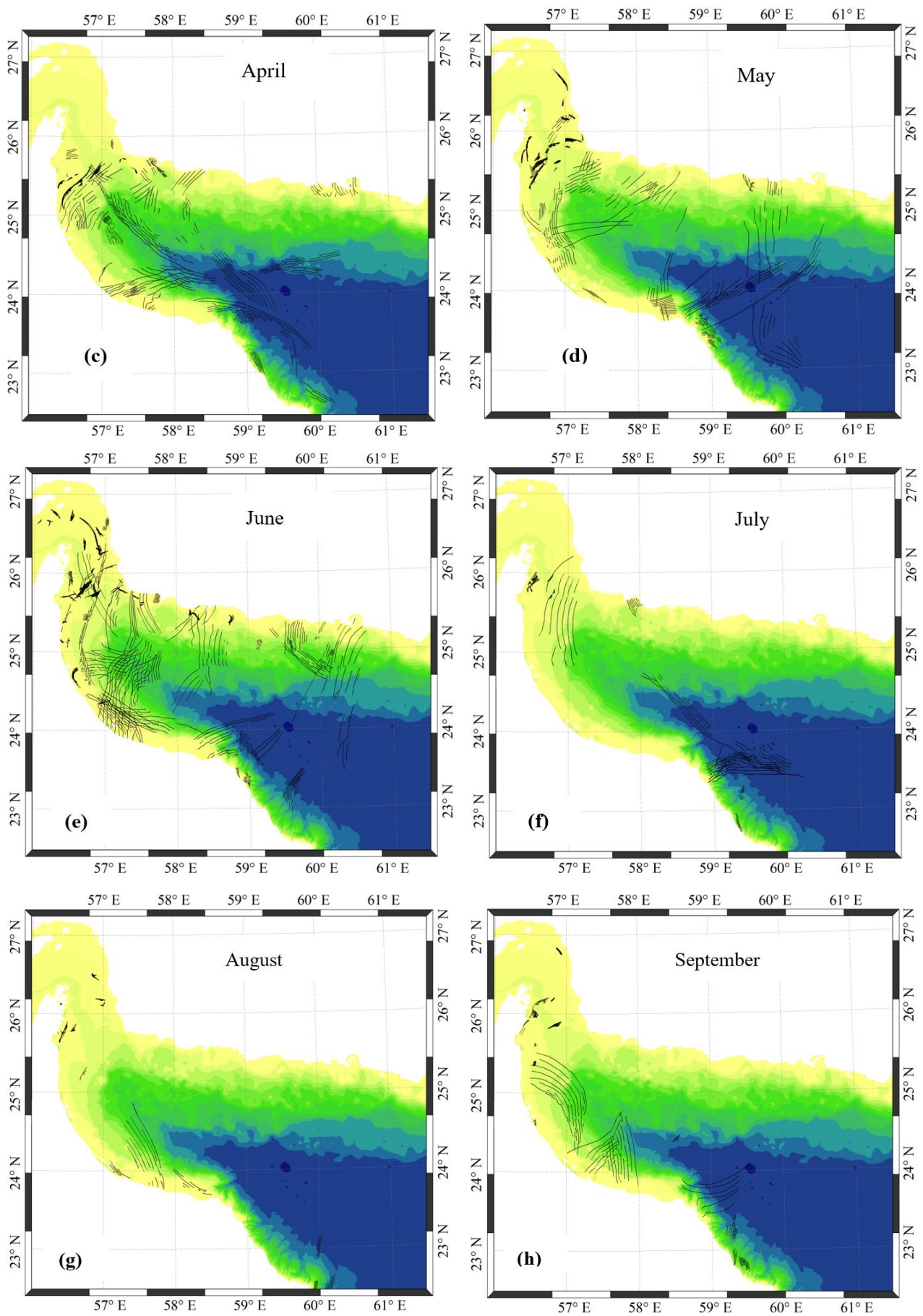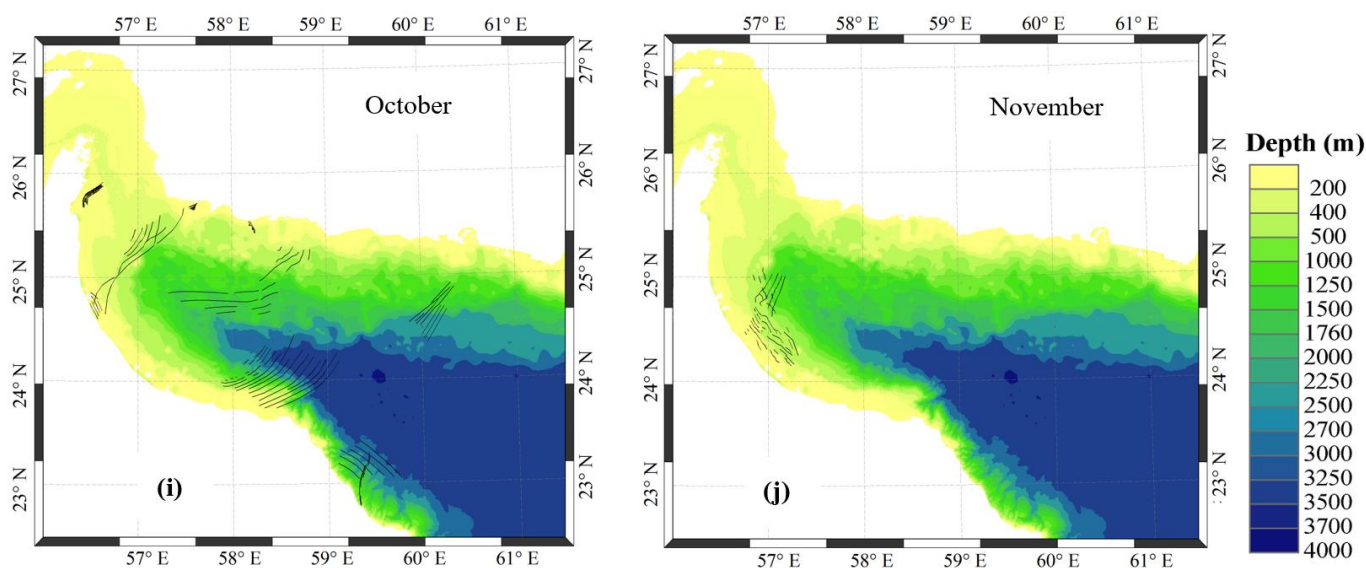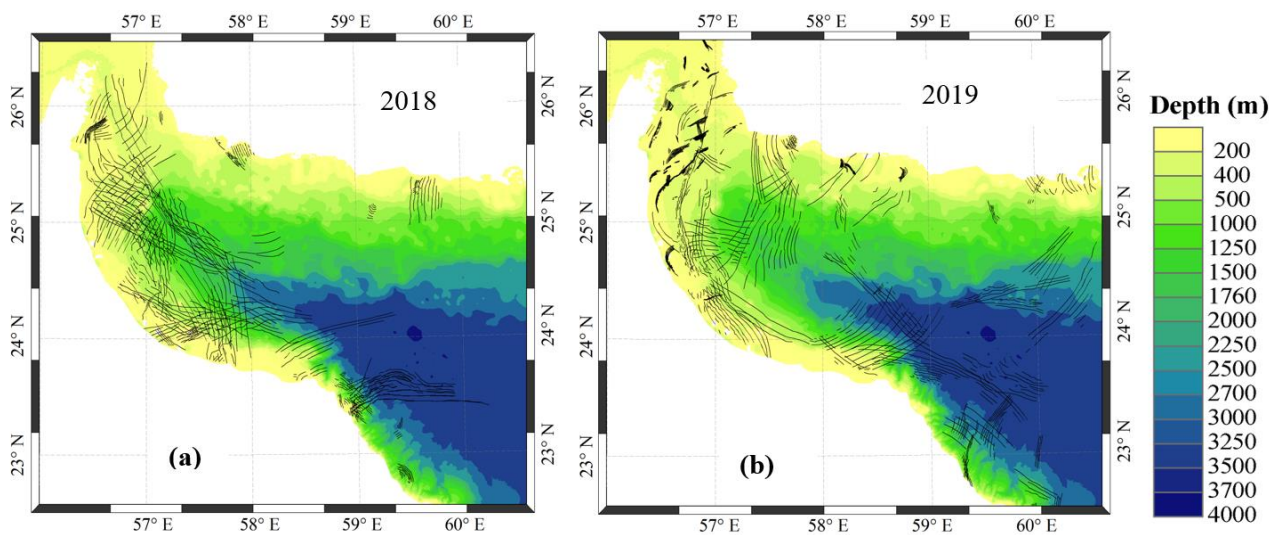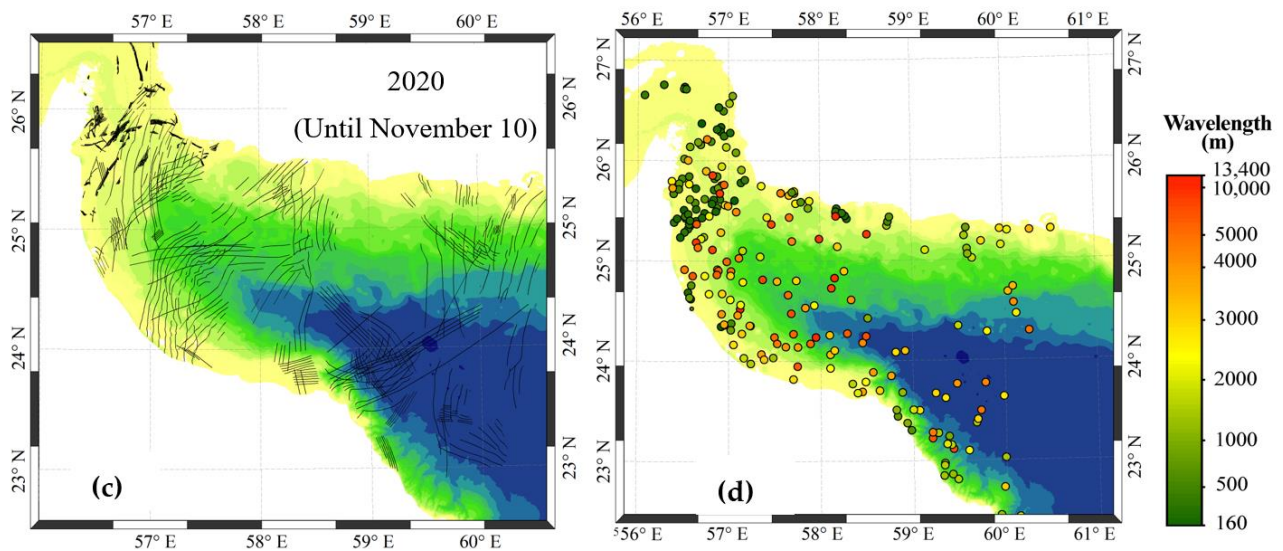
**Figure 3.** Monthly spatial distributions of ISWs from February (**a**) to November (**j**), identified in satellite images. The collection of satellite images encompasses almost 3 years from February 2018 to November 2020. (In all images, the colors illustrate the bathymetry in the GoO and black thin lines show the wave fronts identified in satellite images).

Figure 4 illustrates the annualspatial distributions of ISWs in 2018–2020. In this period, the northern part of the GoO had noticeably lower numbers of ISWs than the western and southern parts. Furthermore, the number of detected waves increased from February to June and decreased from June to November.

**Figure 4.** Yearly spatial distribution of ISWs in the period 2018–2020 (frames (**a**–**c**)) and distribution of ISW wavelengths (frame (**d**)) (The colors illustrate the bathymetry in the GoO and black thin lines show the wave fronts identified in satellite images).

As shown in Section 3.1, there are two major levels of stratification in the GoO during a year. In the first period, which lasts from May to October, $N^2$ mostly exceeds $8 \times 10^{-4}$ $1/S^2$ throughout the basin. In the second period, which lasts for the rest of the year, the stratification either is much weaker or does not exist at all ($N^2$ mostly less than $5.5 \times 10^{-4}$ $1/S^2$). The variability of the depth and stratification in the GoO results in the variation of coefficients in the model equations presented above. In this study, June and April were selected as the representatives of two typical stages of stratification. Figure 5 depicts the scatter plots of the dispersion relations $k$-$\omega$ for the detected ISWs shown in Figures 3 and 4, where $k$ is the wavenumber and $\omega$ is the frequency of ISWs. It is worth noting that only the crests having a distinct quasi-linear pattern were considered in the calculation of the dispersion relation. All detected wave packets can be conditionally separated into two groups, (i) those which were detected in the deep regions where $kh_2 > 2$ and (ii) those which were detected in the shallow regions where $kh_2 < 2$. The best-fitted curves for these data are presented in Figure 5 by dashed lines.
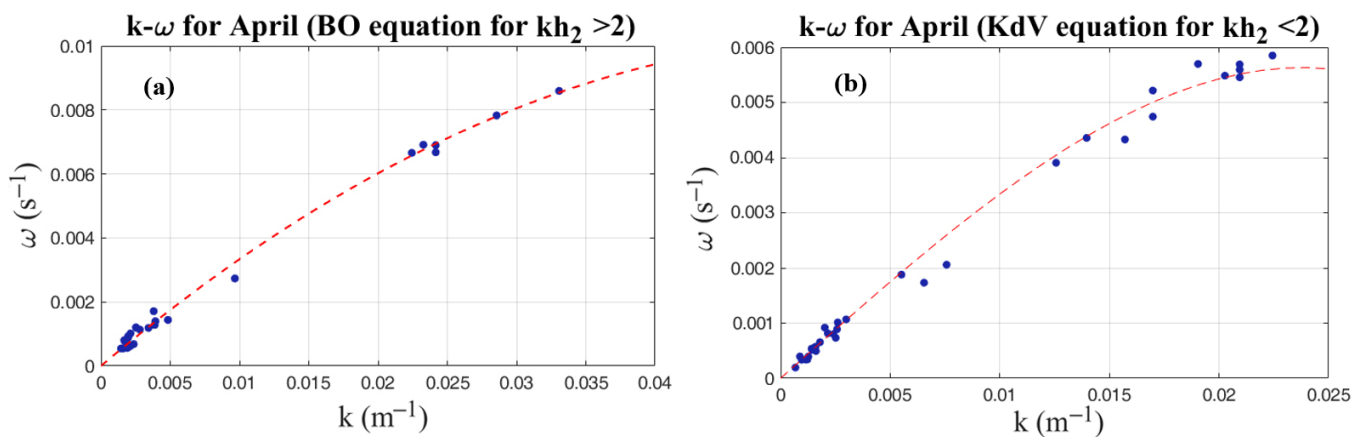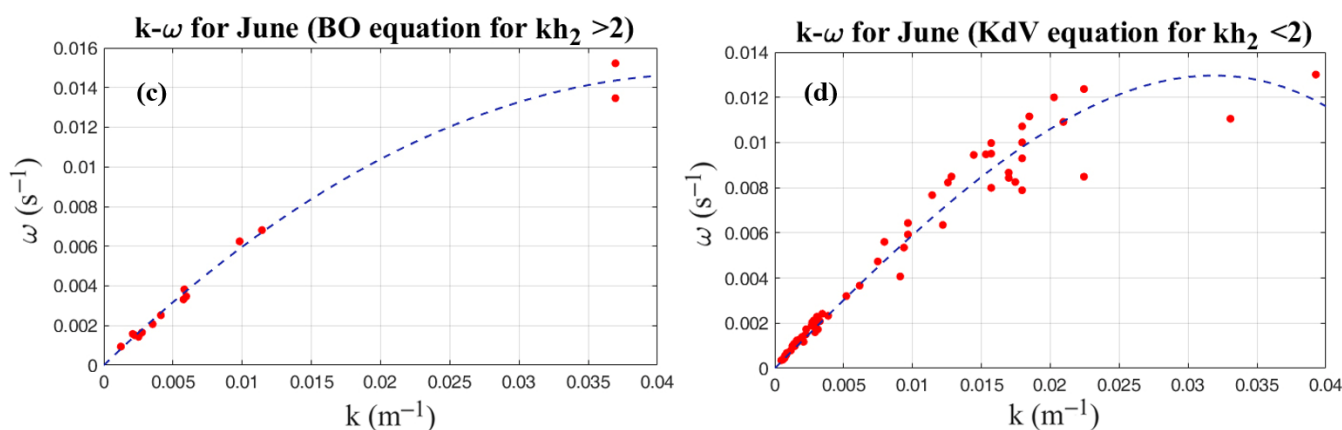
**Figure 5.** Dispersion relations in terms of $k$-$\omega$ scattered data and the best-fit curves for ISWs in April (**a**), (**b**) and June (**c**), (**d**). (**a**), (**c**) show data fitting by quadratic polynomials suitable to the BO Equation (7), and (**b**), (**d**) show data fitting by cubic polynomials suitable to the KdV Equation (6). Here $h_2$ is the thickness of the lower layer.

Moreover, Table 1 shows the model equations and corresponding dispersion dependences as shown in Figure 5. The wavenumbers were determined from the satellite images of wave packets and frequencies were calculated using Equations (6) and (7). In June, the values of the linear wave speed ($c$) and dispersion parameter ($\beta$) attained 0.61 m/s and 200 m³/s, respectively, whereas, in April these quantities were 0.36 m/s and 209 m³/s.

**Table 1.** Dispersion relations for ISWs in the GoO.

| Month | Condition | Equation | R² |
|---|---|---|---|
| April, weak stratification | $kh_2 > 2$ (BO) | $\omega = 0.366k - 3.262k^2$ | 0.9945 |
| | $kh_2 < 2$ (KdV) | $\omega = 0.355k - 208.8k^3$ | 0.991 |
| June, strong stratification | $kh_2 > 2$ (BO) | $\omega = 0.675k - 7.744k^2$ | 0.992 |
| | $kh_2 < 2$ (KdV) | $\omega = 0.610k - 200k^3$ | 0.962 |

As expected, the phase speed is considerably higher in June when stratification is strong. High values of the coefficient of determination ($R^2$) shown in Table 1 demonstrate a highly reliable prediction of the derived equations for both deep and shallow regions. The spatial distributions of coefficients of the JKKD equation in April, June, and September are shown in Figure 6.
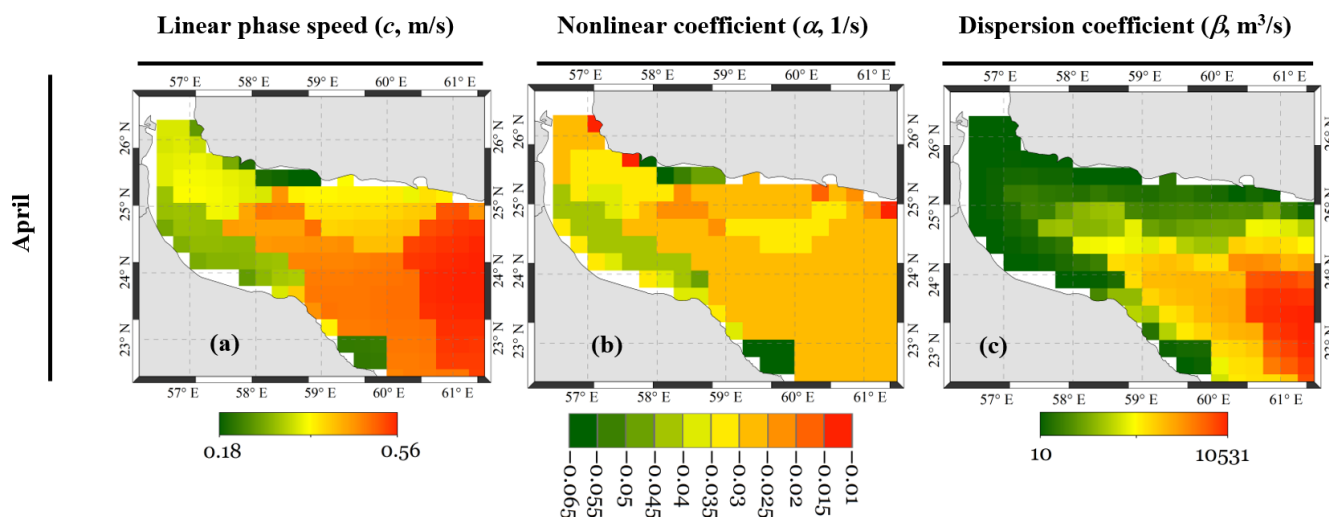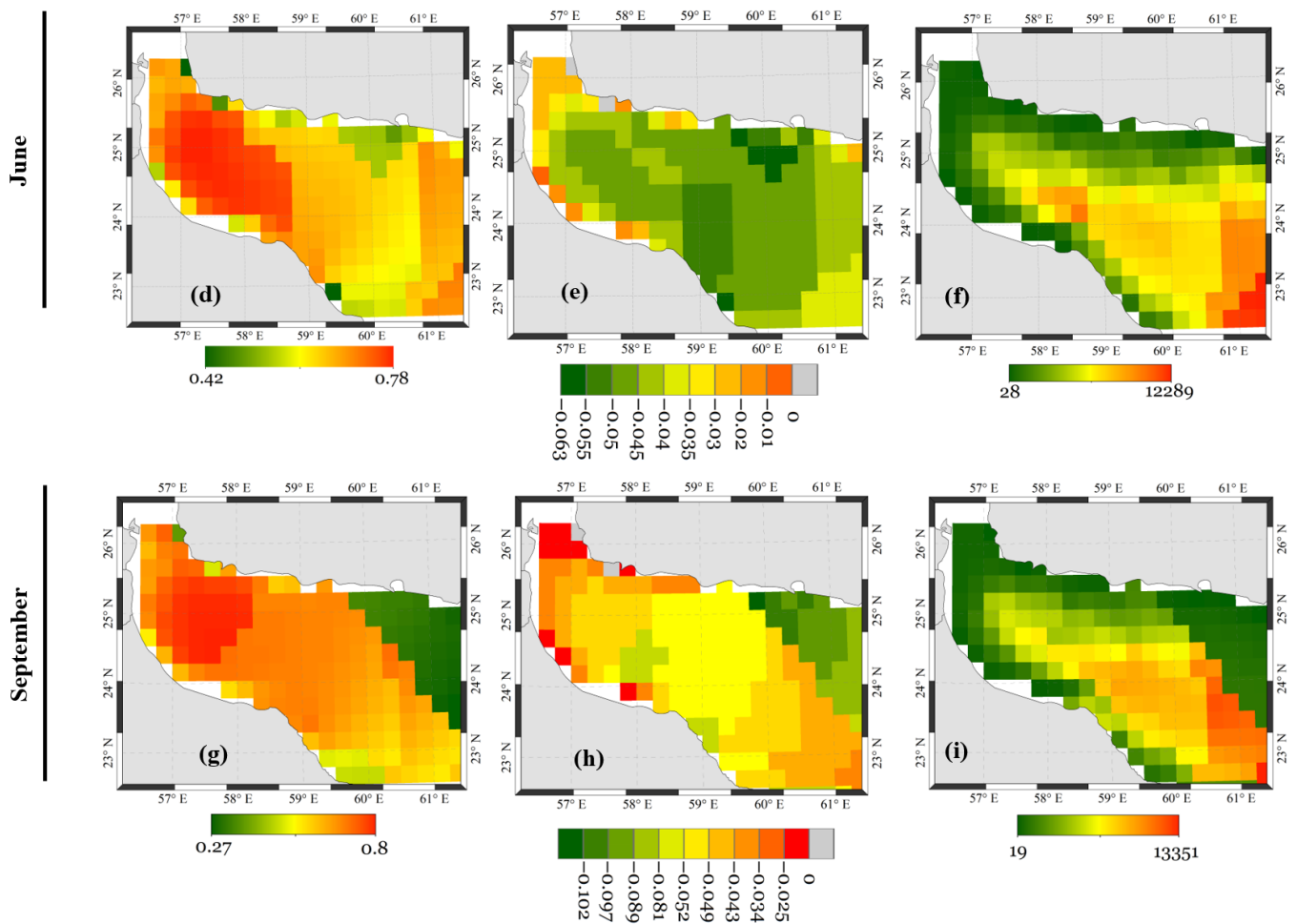
**Figure 6.** Coefficients of the JKKD equation in the GoO in April (**a**–**c**), June (**d**–**f**), and September (**g**–**i**).

It should be noted that the JKKD coefficients were calculated using WOA profiles; however, two main factors may cause small deviations of calculated coefficients from the genuine values. Firstly, WOA datasets pertain to long-term averaged data that may not necessarily represent the real hydrological condition at the time when a specific ISW packet was detected. However, owing to the fact that external forces that may make abrupt changes in stratification (such as cyclones) rarely occur in this area, the yearly cycle of stratification is almost persistent in the GoO. Secondly, WOA lacks data near coastlines and therefore some discrepancies are expected for the coastal zones. Nevertheless, as will be shown below, the mentioned factors will not cause noticeable defects in estimations.

## 4. Mechanisms of ISW Generation in the GoO and Zonal Analysis

In this section, we examine different driving mechanisms of ISW generation in the GoO and present examples of each mechanism. Evaluation of the detected waves regarding their shape, propagation direction, wavelength, and crest length, in addition to the location, depth, and frequency of the events suggests that they are generated by different mechanisms. Some of the mechanisms can be simply identified using characteristics of observed waves and local bathymetries. As mentioned before, tidally generated ISWs in the GoO have been previously studied to some extent, and their main characteristics have been discussed in the papers (See [36,39,40]). Such waves are mostly generated at the tidal peaks and, consequently, the time of generation is definite for this type of ISWs in the GoO. Moreover, they are generated in specific locations and have an almost persistent propagation direction.

However, there are many other cases that cannot be simply analyzed in terms of the mechanisms that were responsible for their generation. These types of ISWs have long wavelengths (from 1 km to more than 10 km), occur in any crest shape and length, and are generated in different parts of the GoO. To find the exciting force of this class of packets, it is required to estimate the time of generation of each observed packet and then analyze possible forces capable of causing such an event at that time. Each force (or forces) that is in a good correlation with the spatial characteristics of the packet (location, propagation direction, etc.) is considered the possible driving force. Therefore, the first challenge is to determine the time of generation for each wave packet.

To estimate the time of generation of a packet, a simple calculation method based on the dispersion characteristics presented in Section 3 is deployed. The main contribution to the ISW traveling speed is made from the linear phase speed, $c$, with a possible non-linear correction up to 20% (such a big correction can be still consistent with the weakly nonlinear models). We, however, assume that the speed of the leading solitary wave in the packet is 10% greater than the speed of long linear waves, $V = c(1 + 0.1)$. The distance of the leading wave crest from the coastline is the maximum possible distance traveled by the wave; therefore, the maximal time of soliton propagation from the coast is $t_{max} = d_{max}/V$. Figure 7a illustrates the typical wave packet. If we denote $t_{img}$ as the time when the satellite image was taken, then $Gt = t_{img} − t_{max}$ will be the rough estimation of the generation time of the packet. It is worth noting that such a calculation is not able to calculate the exact time of generation and is performed only to find a reasonable time moment when the packet could be generated. The next step is to look for the possible driving forces that existed around time $Gt$.
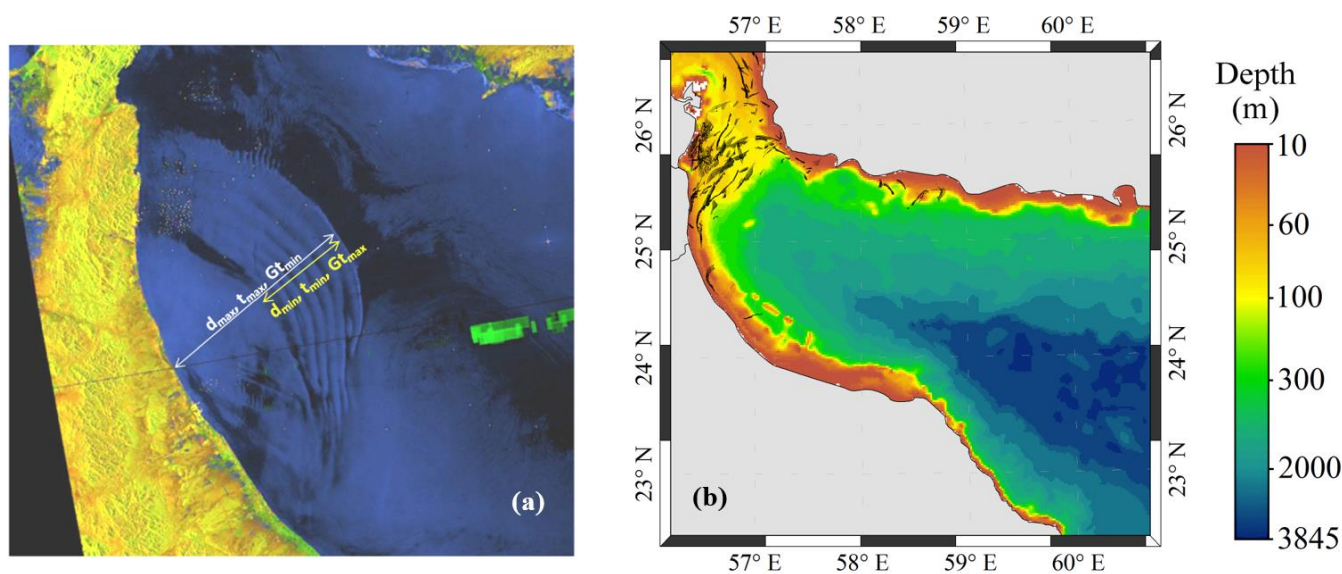


**Figure 7.** (**a**) Definition of the parameters for the calculation of time when the wave packet was generated. Sentinel-1 image was taken on 30 September 2019 at 14 h 17 min. The parameter $d_{max}$ is shown which was used for the calculation. (**b**) Tidally generated ISW packets (black strips) observed from 2018 to 2020. Tidally generated ISWs usually appear when the tide reaches its daily maximum or minimum (black thin lines show the wave fronts in the right panel).

### 4.1. Tide

One of the potential exciting forces of ISW generation is the tide. By evaluating the ISWs and their characteristics identified in the GoO, it is revealed that, owing to the regular tide appearance, tidal variations can contribute to generation of ISWs in specific areas and have similar characteristics including regularity, wavelength, speed, propagation direction, etc. Examples of tidally generated ISW packets observed from 2018 to 2020 are shown in Figure 7b. According to this figure, these types of ISWs usually occur from

April to September on the western shelf as well as along the southern coast of the GoO with wavelengths ranging from 200 to 500 m.

Therefore, there is a fairly simple way to determine the time of ISW generation through this mechanism. The definiteness of the generation time of this class of ISWs enables us to calculate their phase speeds based on their observed characteristics in the satellite image (which shows the real situation) and compare with that of the estimated using WOA datasets representing the long-term averaged stratification conditions in the GoO. However, the traveling distance of the leading crest is also required to calculate the wave speed $V = d/t$. To determine the traveling distance, $d$, for a packet, a simple geometrical scheme was deployed according to the surface patterns of the ISW packet shown in Figure 8.
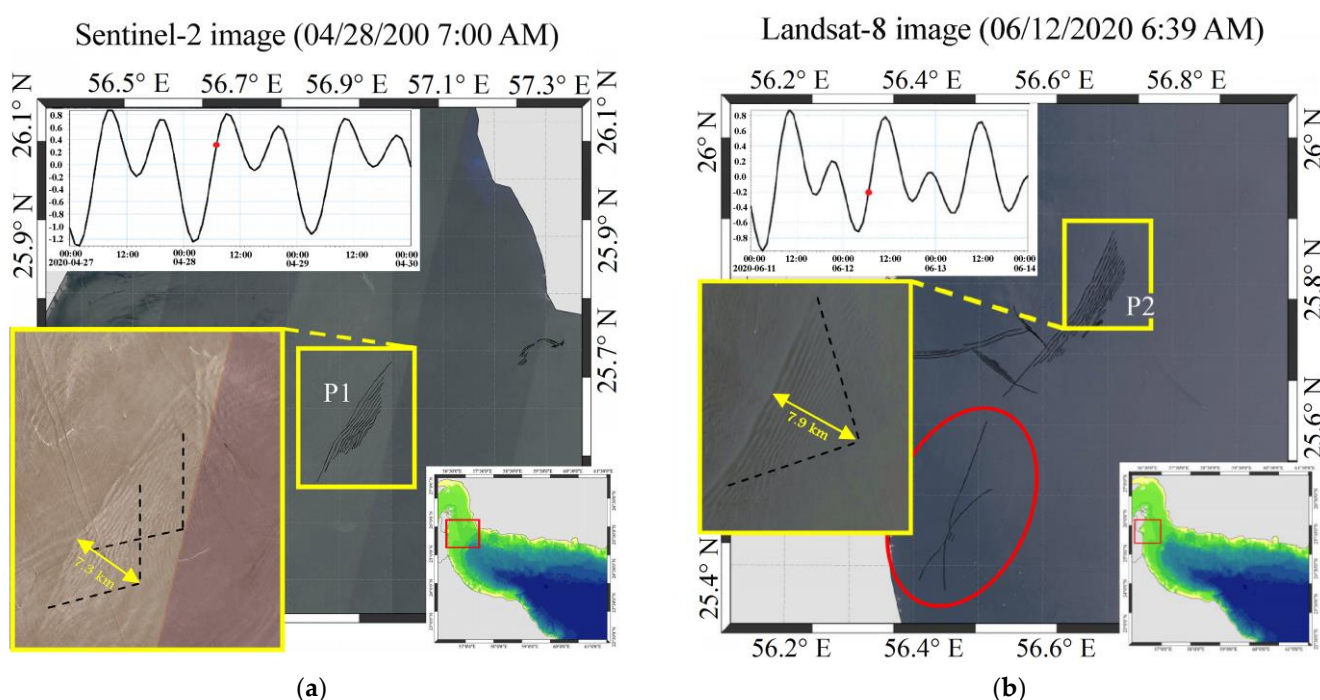


**Figure 8.** ISWs generated by a tide on the western shelf of the GoO. (**a**) Sentinel-2 image taken on 28 April 2020 at 7:00 a.m.; (**b**) Landsat-8 image taken on 12 June 2020 at 06:39 a.m. The plots on the upper left corner of each image show the tidal elevation, and red dots mark the capturing time of each satellite image (black thin lines shows the wave fronts in all images).

This figure illustrates two tidally generated packets, P1 and P2. The surface signatures of the consecutive crests clearly show the triangle shape patterns that can be used to determine the starting point of each packet. Therefore, the distance $d$ can be simply measured as the distance between the focal points and leading crests. According to this approach, the traveling distances of the packets P1 and P2 are measured to be 7.3 km and 7.9 km, respectively. Moreover, the traveling times of the packets (the time difference between the low tide and capturing time of the satellite image) are 5 h and 3.67 h; therefore, the traveling speeds of the packets P1 and P2 are calculated as 0.41 m/s and 0.6 m/s, respectively. A comparison between these values with those predicted from the KdV dispersion relations in Table 1 for April and June ($c_1 = 0.36$ m/s and $c_2 = 0.61$ m/s) demonstrates a satisfactory accuracy of the suggested method of estimation.

In Figure 8b, one can see also in the red oval an H-type interaction of two internal solitary waves in terms of [41]. The resultant effect of the nonlinear interaction of solitary waves depends both on their amplitudes and the angle at which they cross [42,43]. In the case when the crossing angle is not too big, as in Figure 8b, backward spatial phase shifts occur in both solitary waves. The amplitude of the resultant stem wave (the bridge be-

tween incoming and outcoming wave fronts) in some models can reach up to four times of amplitude of each wave (see, e.g., [41,43]; and references therein). Such amplification can cause wave breaking and enhance mixing near the coasts. As mentioned by Jackson et al. , it can also provide massive forces exerting on offshore structures [44].

A barotropic tide after reflection from the steep coasts partially transforms into the baroclinic tide which can also initiate a secondary mechanism of ISW generation in the process of evolution. This mechanism of generation is mainly typical along southeastern coastlines of the GoO where a steep bed with almost no shelf exits and ISWs with wavelengths of about 1 km are usually observed propagating seaward (see Figure 9).
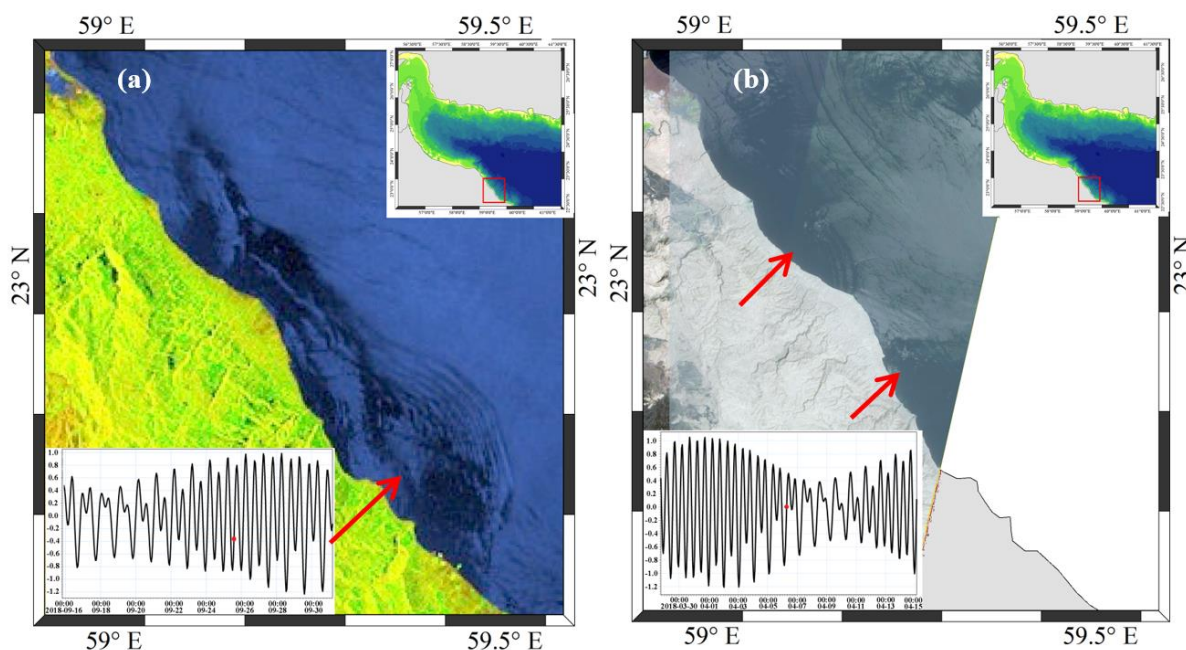


**Figure 9.** ISWs potentially generated by the tide reflected from the coast, identified in (**a**) Sentinel-1A image taken on 25 September 2018 at 2:07 p.m., and (**b**) Sentinel-2 image taken on 6 April 2018 at 6:50 a.m. The plots on the lower left corner of each image show the tidal elevation and red dots mark the capturing time of each satellite image.

### 4.2. Lee Waves

The generation of ISWs resulting from the interactions of local currents with an underwater sill has been well evaluated in several studies (See Section 1). Although this mechanism has been well documented in other basins all over the globe and studied using observational and numerical methods, it has not been reported and studied in the GoO yet. This mechanism could be potentially active on the northern and southern shelves where the bathymetry becomes more intricate with underwater shoals. According to the identified packets in these regions, the sill-generated ISWs are characterized by wavelengths in the same order as tidally generated waves (usually less than 500 m). They regularly manifest at the same locations and have irregular shapes complying with the shape of the sill. A sill peak should be sufficiently shallow (20 to 50 m) to run this mechanism in the GoO, and the direction of propagating of the resultant ISWs depends on the direction of the local current hitting the sill (see Figure 10).
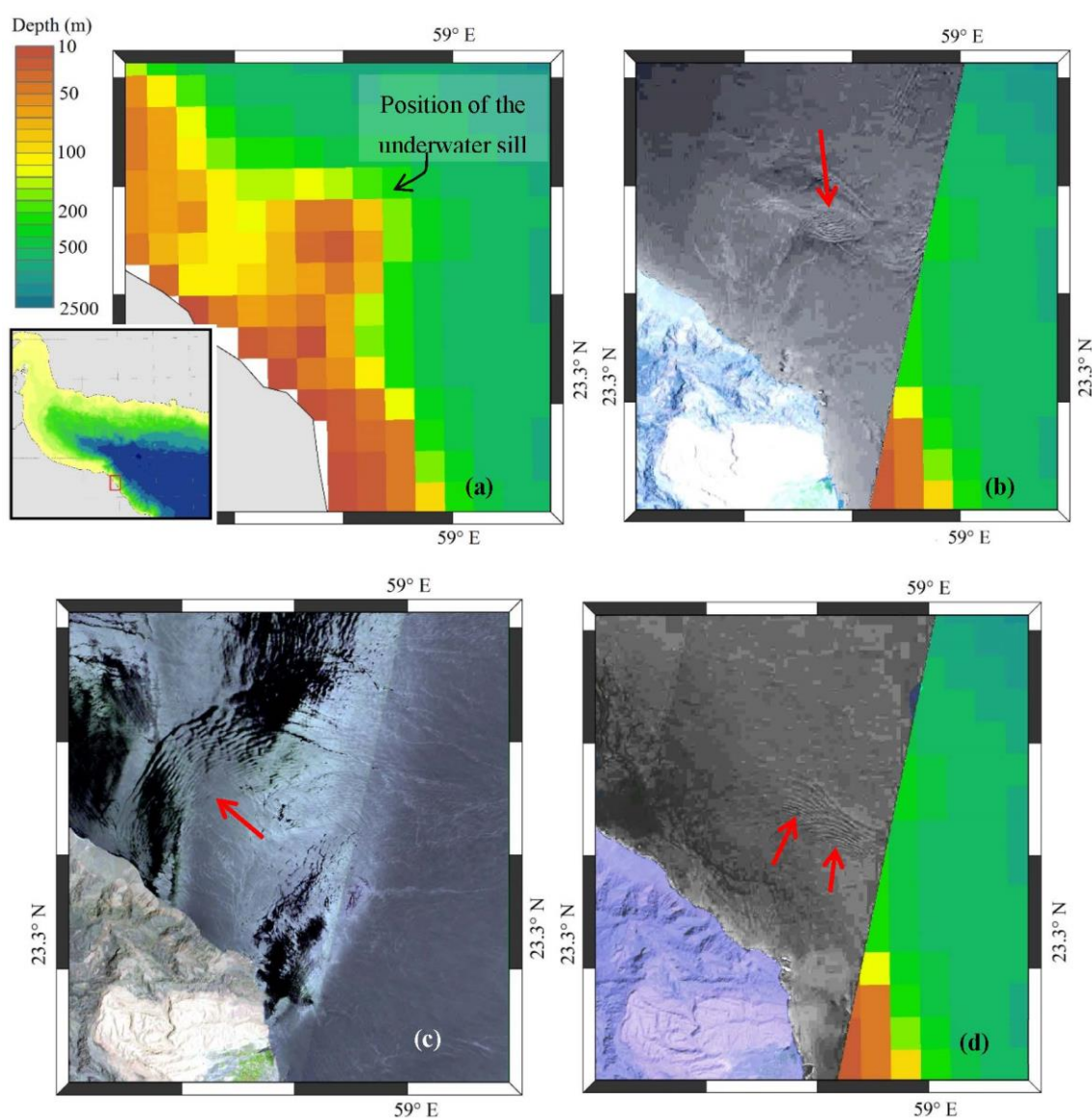
**Figure 10.** ISWs generated by the sill–current interaction. Frame (**a**) shows the bathymetry and location of the underwater sill; frames (**b–d**) depict ISWs generated by the sill–current interaction and propagating toward various directions depending on the current direction. Red arrows show the ISWs and their directions of propagation.

### 4.3. Atmospheric Perturbations

In addition to the ISWs described above, other ISWs were observed with big wavelengths, long crest lengths, and irregular crest shapes. Apparently, they cannot be attributed to the tide due to their location, wavelength, shape, propagation direction, SAR intensity, and, more importantly, the irregularity of their occurrences. The crest lengths and spatial periods of these waves suggest that, first, a source of considerable energy is required for their generation and, second, the source affects a significant part of the basin (see Figures 3 and 4). Another reason that they cannot be attributed to the tidal forces is that these events are considerably diverse in the shape, occupied area, and direction of propagation. However, the processing of satellite images together with the atmospheric datasets suggests that such large ISWs were potentially generated by atmospheric perturbations. For these kinds of ISWs in the GoO, the equation for *Gt* as per Section 4 can be used to estimate the time of their generation and, consequently, find the source of perturbation.

Figure 11 illustrates a Sentinel-1 image taken on 1 July 2019 at 2:00 a.m. ($t_{img}$) with several long-crest waves propagating toward SW. The distance between the packet and the NE coastline was too big, and it was unreasonable to use it for the estimation of the traveled distance. However, the analysis of meteorological charts shown in Figure 12 revealed that a persistent convergent wind field existed on 30 June from 8:00 to 16:00 over the basin of GoO with the shape capable of generatingthe observed ISWs.
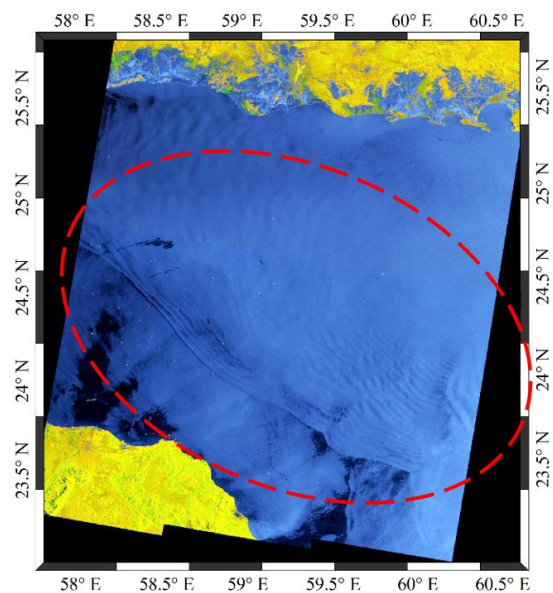


**Figure 11.** Sentinel-1 image taken on 1 July 2019 at 2:00 a.m. The parameter *d* is shown that was used for the calculation. Dashed lines encompass the active wind area in the GoO on 30 June 2019.
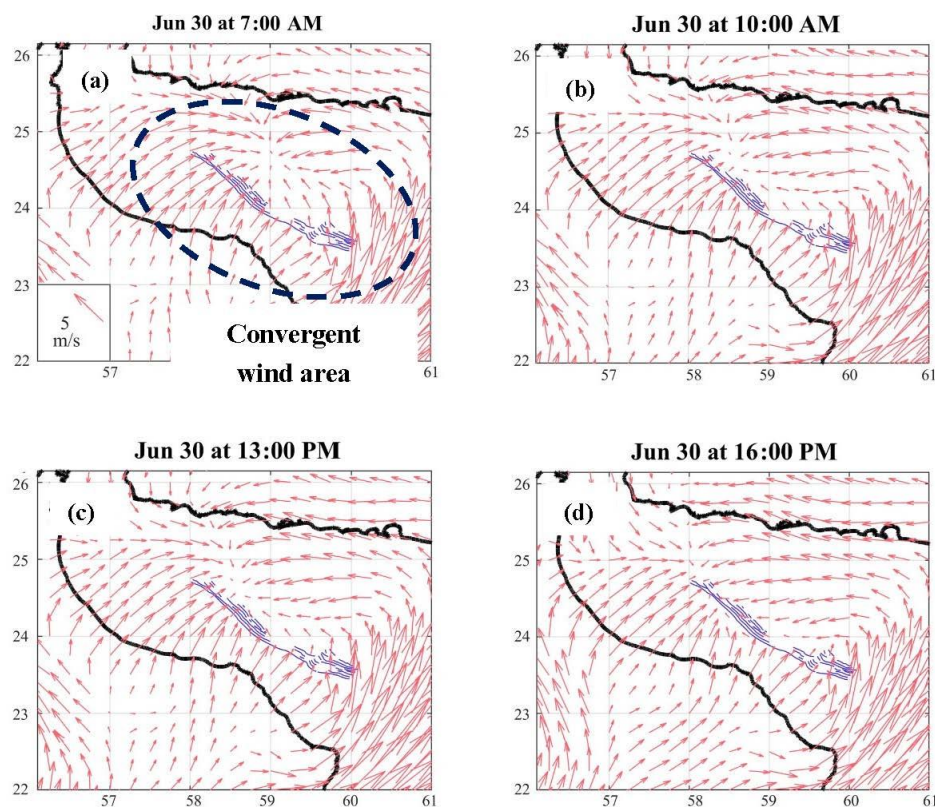


**Figure 12.** Wind field over the GoO on 30 June 2019 from 08:00 to 16:00 local time. The location of the observed packet has been overlaid as blue lines to clarify the mechanism of ISW generation. The

dashed line ellipse shows the zone of wind convergence where the atmospheric pressure increases. Blue thin lines show the wave fronts in all images just to show the location of the ISWs in the satellite image shown in Figure 11.

The distance between the localization of the wind source and the leading solitary wave can be roughly estimated as $d_{min}$ = 22 km. Using the wave speed $c \approx 0.61$ m/s for the KdV model in Table 1, we can estimate the time $t \approx 10$ h of solitary wave observation at its position on the image. This time well-correlates with the time when the satellite image was taken on 30 June 2019 at 16:00 p.m.

### 4.4. ISWs Generated by Eddies

One more driving mechanism which could mainly be active in the western and southern zones of GoO runs by eddies. Eddy-induced ISWs in the GoO are usually generated in shallow regions with wavelengths less than 1000 m, according to satellite images. Since the depth of the thermocline is modified in the presence of eddies, averaged values of water column properties may not properly represent the condition at the location of eddies. In other words, field observations are essential for a precise quantitative analysis of this mechanism. Figure 13 depicts a Sentinel-2 image on the western shelf of the basin (taken on 29 April 2018 at 7:00 a.m.) including a dual eddy system with the same polarity which generated ISWs in-between and in the outer region of this system. The wavelength of generated waves in the inter-eddy zone is noticeably smaller than in the outer area. The observed characteristics correlate with those reported by Sandven and Johannessen ,and Johannessen et al. [22,23].
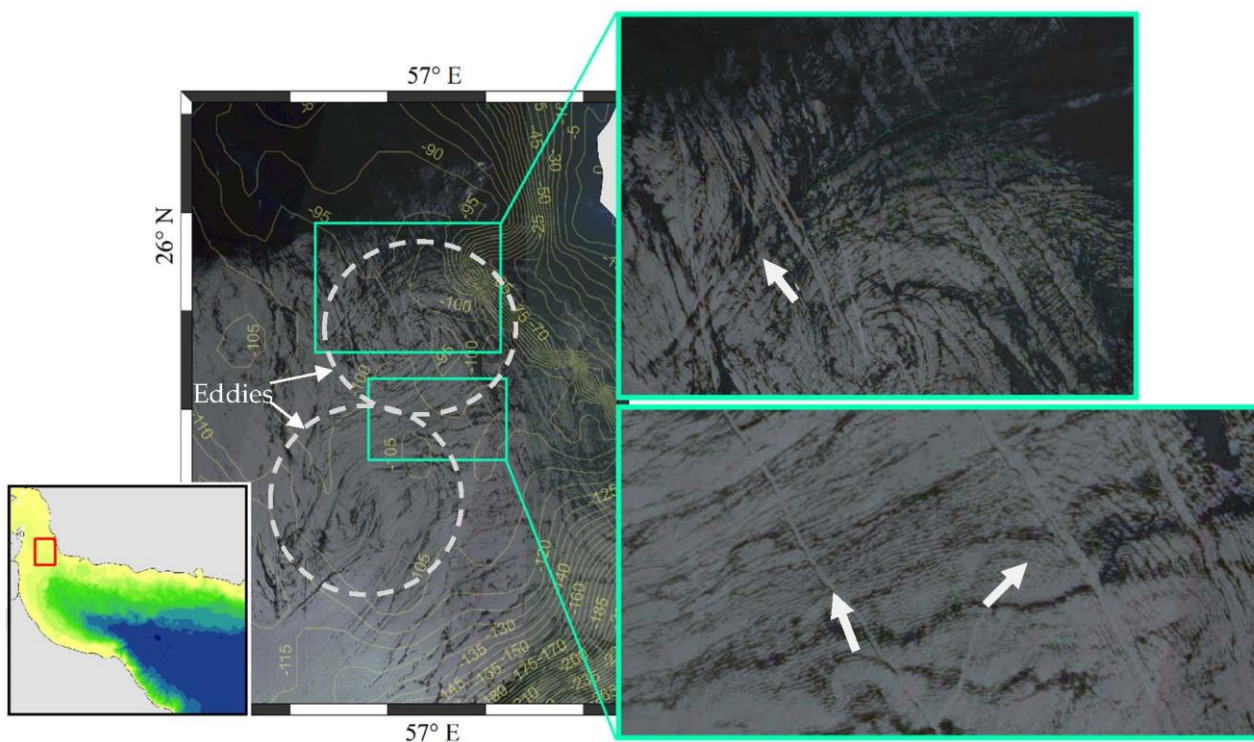


**Figure 13.** Sentinel 2 images taken on 29 April 2018 at 7:00 a.m. depicting a dual eddy system and the eddy-induced ISWs. The white arrows indicate the generated ISWs and their propagation direction. The depth contours have been shown as yellow lines in the satellite image. The red rectangle illustrates the area shown in the satellite image.

### 4.5. Other Mechanisms

Figure 14a shows a TerraSAR-X image taken on 16 June 2019 at 2:15 a.m. Two wavetrains of ISWs, as well as a wavetrain in the lee side of the Jask headland, can be observed. For the wave packets P3 and P4 propagated almost parallel to the coastline, it was not possible to determine the distance $d$ to the source of generation. However, it is obvious from the image that the generation domain was affected by the atmospheric perturbation located on east of the captured area.
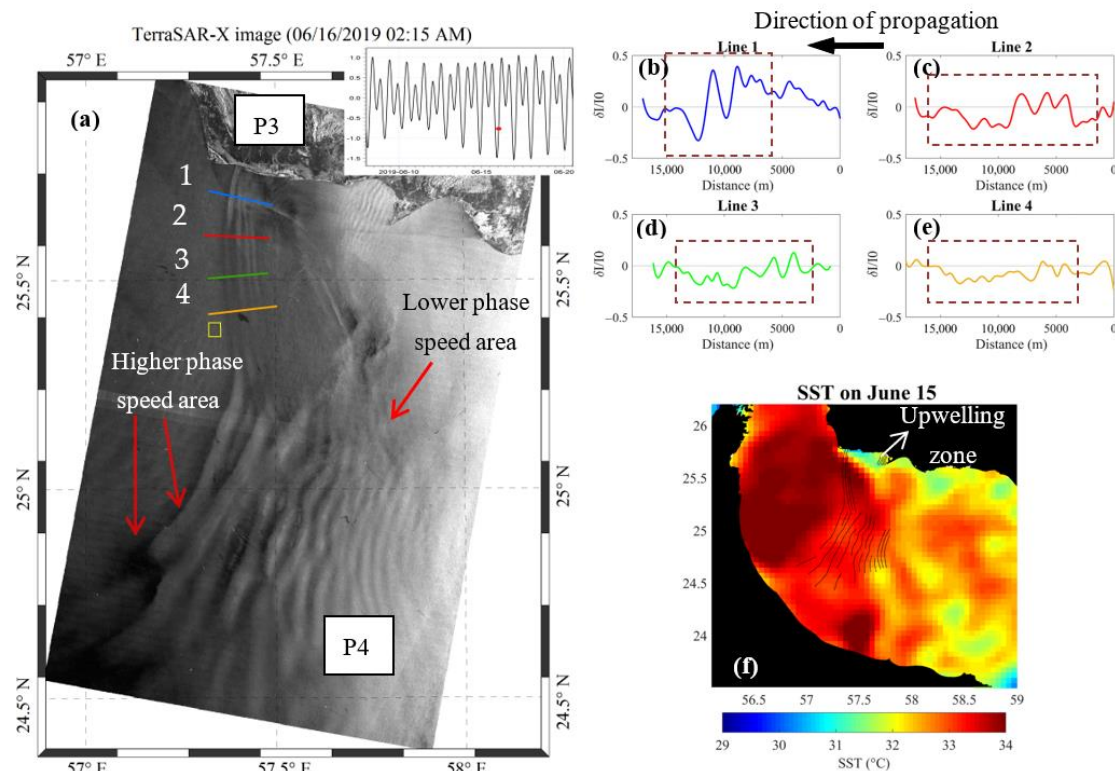


**Figure 14.** (**a**) TerraSAR-X image taken on 16 June 2019 at 2:15 a.m. The plot on the upper right insertion shows the tidal elevation, red dot marks the time when the image was taken. A small yellow square shows the area used to calculate the background backscatter. (**b–e**) Relative SAR intensities along the lines from 1 to 4; (**f**) sea surface temperature (SST) distribution on 15 June 2019 from the satellite Copernicus (black thin lines in (**f**) represent the location of ISWs in (**a**)).

Figure 15 shows the pressure field in the GoO on 14 June 2019 from 1:00 to 12:00 when a moving high-pressure field with the same characteristics (e.g. travelling direction and spatial pattern) as the observed packets emerged. To further discuss packet P3, it is required to take a closer look at the complicated atmospheric and hydrodynamic conditions of this region on 15 and 16 June 2019.
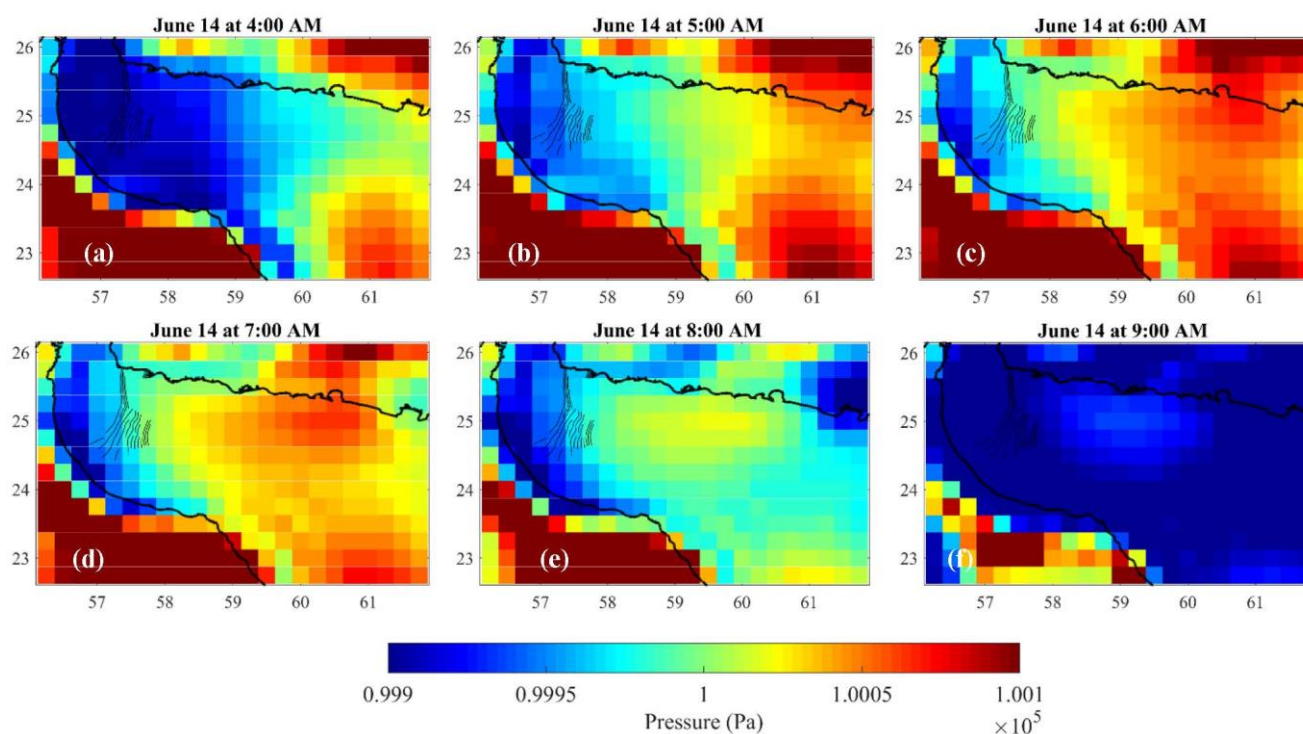
**Figure 15.** Pressure field in the GoO on June 14 from 4:00 a.m. to 9:00 a.m. Wave crests in the satellite images are shown by solid black lines in all graphs to make the generation progress clearer (black thin lines in all figures represent the location of ISWs in Figure 14a).

The tide was at an extreme level since approaching the spring tide which occurred on 18 June 2019. Moreover, upwelling was taking place in the coastal area as shown in Figure 14f, and a divergent wind field was also prevailing in the area on 15 June 2019 from 14:00 to 18:00 (see Figure 16 below). On the other hand, a barotropic Kelvin-type surge resulting from cyclone Vayu existed in the area with a traveling speed of about 4 m/s. In this region, the surge commenced rising at the beginning hours of 15 June 2019 and reached a peak in the middle of 16 June 2019 (see Figure 17b). Unfortunately, there is no field data to survey the structure of this surge; however, Koohestani et al. studied the characteristics of another surge, driven by cyclone Ashobaa in 2015, which was associated with a substantially strong westward current along the northern coasts (higher than 1 m/s at a point located near Chabahar Bay at 30 m depth) [28].
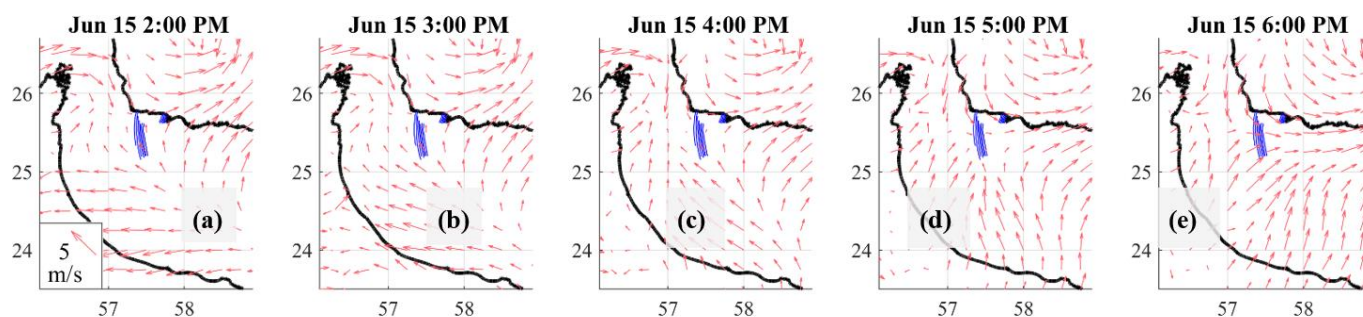


**Figure 16.** Wind field (red arrows) on 15 June 2019 from 14:00 to 18:00. The location of the packet P3 (See in Figure 14a) has been overlaid as blue lines in all panels to clarify the mechanism of ISW generation).
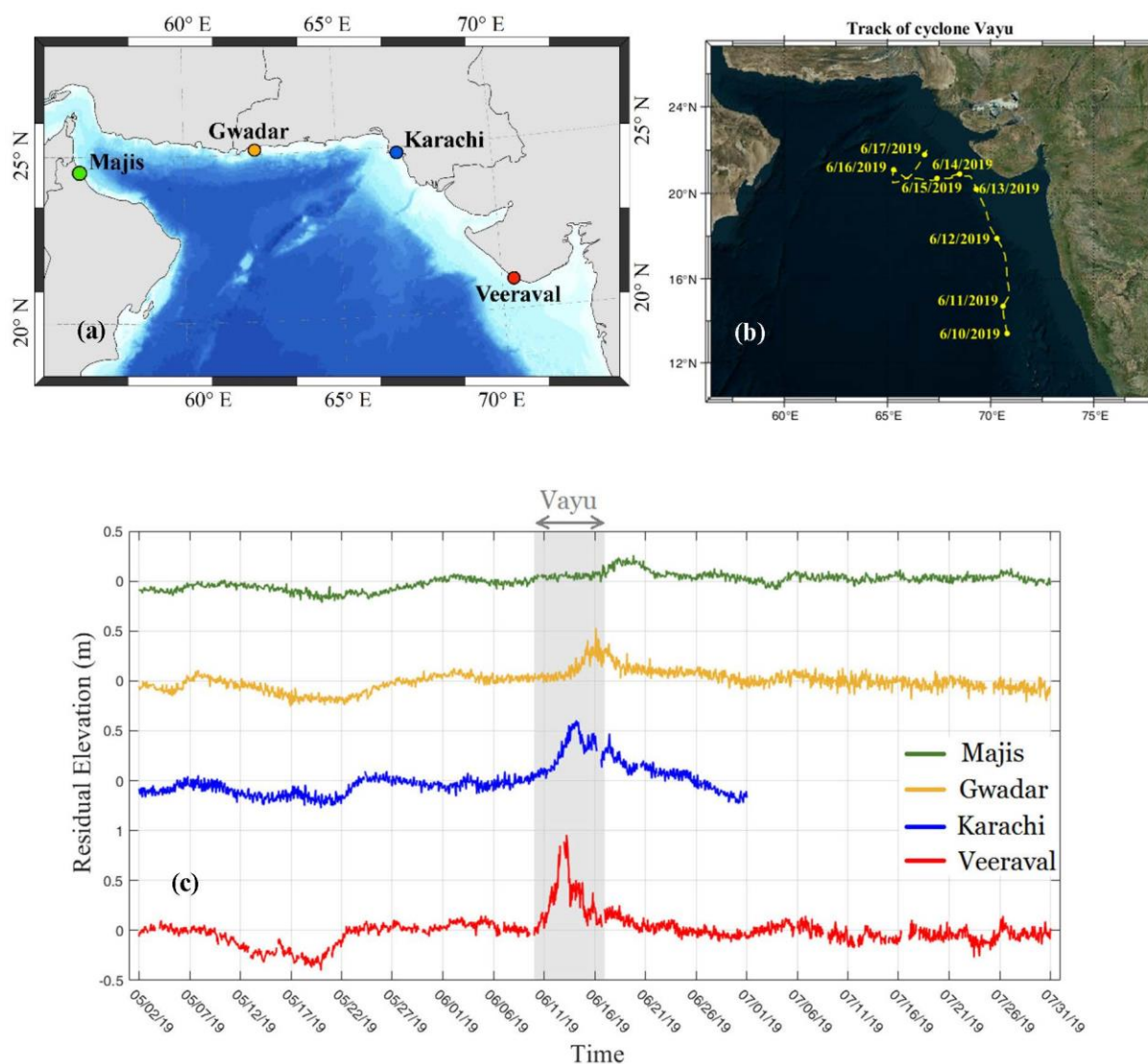
**Figure 17.** (**a**) Positions of stations for sea level measurements. (**b**) Track of the cyclone Vayu on 15 June 2019. (**c**) Variations of the sea level measured at different stations. Grey strip in the center shows the time interval of cyclone Vayu manifestation.

On the other hand, the daily mean current field on 15 and 16 June 2019 from the product GLORYS12V1 provided by the Copernicus Marine Environment Monitoring Service (CMEMS, https://marine.copernicus.eu, accessed on 5 July 2021) indicates this surge which associates with a speed of about 0.4 m/s at 0.5 m depth around the packet P3 [45]. It also reveals a strong eddy at the western shelf slope of the GoO which makes the hydrodynamic condition at this area at the time of evaluation more complicated (see Figure 18). Regarding the information provided above, it is deducible that packet P3 was mainly generated by the divergent wind field but with undeniable contributions of other factors.
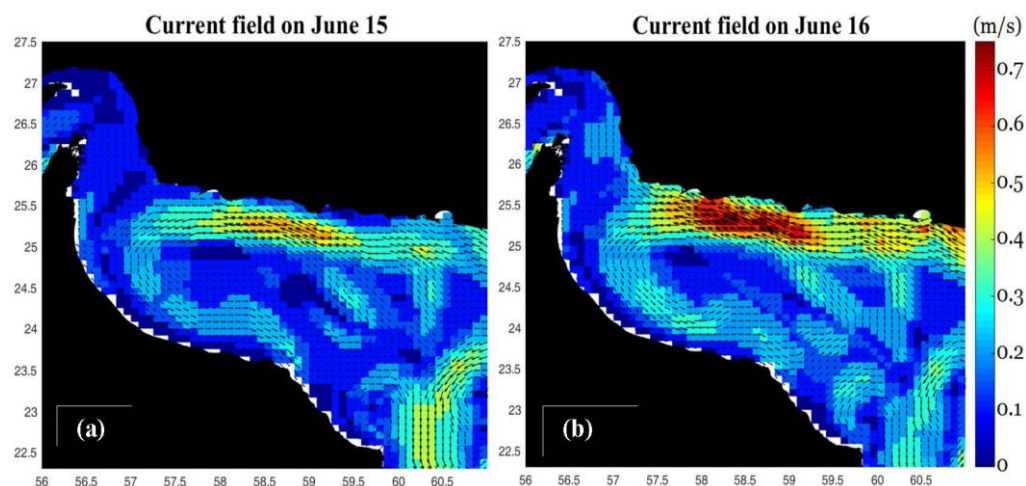
**Figure 18.** CMEMS current fields on 15 and 16 June 2019 in the GoO at the depth of 0.5 m.

Furthermore, Figure 14b–e depicts relative SAR intensities (RSI) along lines 1 to 4 shown in Figure 14a. A small yellow square in Figure 14a shows the area considered as the background backscatter. The RSI values along line 1, which is located near the coast, show a double sign intensity with a dark-leading bright pattern for the leading wave. This pattern takes place in the case of either an elevated type of ISW or a mode-2 ISW whereas the former usually governs in shallow regions [44]. Therefore, packet P3 is an elevation type of ISW in the vicinity of the coastline. It is also compatible with the calculations that are illustrated in Figure 6 wherein $\alpha > 0$ in June and September in this region which means that $h_1 > h_2$. The transition from a double sign to a single negative sign through lines 1 to 4 is attributed to the existence of surface slicks in this area (See [44,46–48]).

The analysis of the wave train P4 is not as complicated as P3. This train is in the deep region far from the coastline (where the depth is more than 1000 m) where the tide and the surge have insignificant effects. Although there were no measurements to determine the local instant stratification, the SST map on 15 June 2019 depicts that a distinct water mass with a considerably higher SST existed on the western end of the basin, suggesting a much stronger stratification in this area (see Figure 14f). The phase speed, therefore, increased in the direction of propagation. The evaluation of atmospheric data on 14 June 2019 reveals that a traveling high-pressure field started moving westward at 2:00 am and reached the location of the packet at 6:00 am.

According to Figure 4, apparently, there are hotspots of ISW generation in the GoO. Looking at this figure, one can suggest a rough zonation of the GoO area regarding the number and characteristics of ISWs in addition to the regional characteristics of the GoO (physical and hydrological). Figure 19a illustrates the zonation; each zone is characterized by at least one of the mentioned criteria as well as the driving mechanisms. Figure 19b shows the histogram of the distribution of ISW wavelengths demonstrating that ISWs with wavelengths between 2000 m and 5000 m dominate, and the second largest group corresponds to ISWs with wavelengths between 400 m and 2000 m. Zones 1, 3, 4, and 5 are much more active than the others. Moreover, ISWs with wavelengths less than 500 m are common within zones 1, 3, and 4. A summary of zone characteristics is given in Table 2.
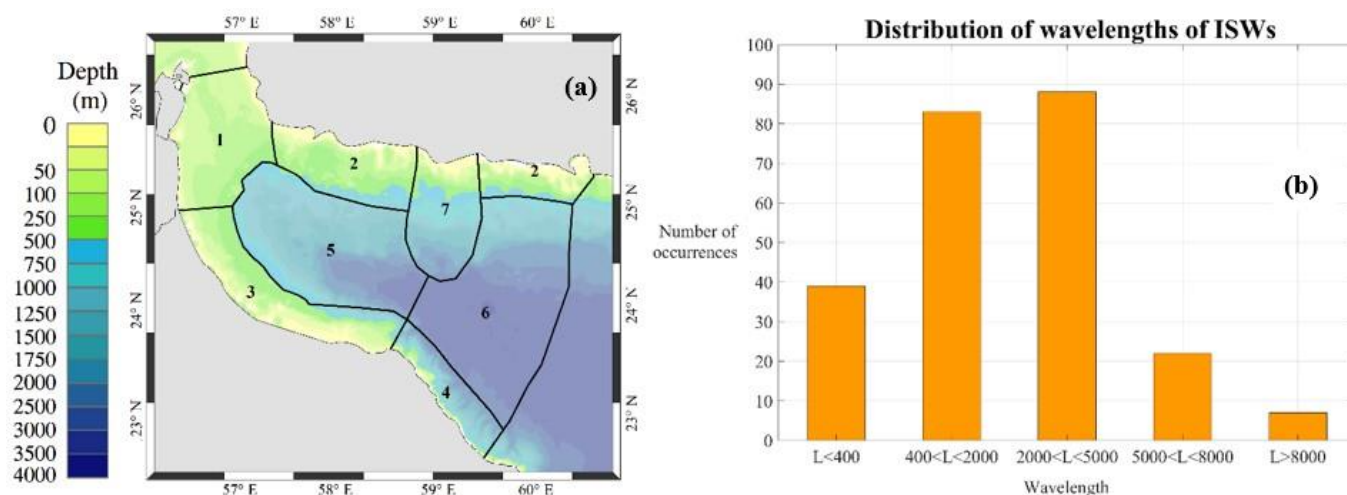
**Figure 19.** (**a**) Zonation of the GoO area where ISWs have different characteristics (for detail see the text). (**b**) The histogram of the distribution of ISW wavelengths in meters.

**Table 2.** Zones and their characteristics in the GoO.

| Zone | Active Mechanisms | Dominant Direction of Propagation | Activity |
|------|-------------------|-----------------------------------|----------|
| 1 | Tide, eddy, current–bathymetry interaction, wind, air pressure | E–W and SE–NW | Very High |
| 2 | Tide, wind, air pressure, current–bathymetry interaction | E–W and NE–SW | High |
| 3 | Tide, wind, air pressure, eddy, current–bathymetry interaction | Various but majorly E–W, NE–SW, SW–NE | Very High |
| 4 | Tide (normal and reflected), eddy, current–bathymetry interaction, air pressure | Various but majorly NE–SW, SW–NE, SE–NW | High |
| 5 | Air pressure, wind | Various | Very High |
| 6 | Air pressure, wind | Various | Low |
| 7 | - | - | Calm area |

*4.6. Characteristics of Detected ISWs*

According to Figures 3 and 4, the number of the detected wave packets varies significantly over a year. At first sight, there is a perfect correlation between the number of observed waves and the strength of stratification. Therefore, the number of detected ISWs increased from April to June and decreased from September to March. However, fewer numbers of ISWs were observed surprisingly from June to September, whereas the stratification intensifies. It may be attributed to either absence of exciting forces (except for tide) or violation of the condition that is required for observing ISWs in satellite images (as is well-known, the Bragg scattering is efficient only at a certain range of a wind speed–see [49]).

To accomplish this, point P shown in Figure 1 (57.75° E, 24.75° N) located in a highly active region is selected as an indicator to be evaluated regarding the atmospheric condition. Figure 20 depicts the hourly mean sea level atmospheric pressure (MSLP) in June 2019 at point P clearly demonstrating a semidiurnal cycle of pressure variation. It is worth noting that a moving pressure field may be characterized as fast and intense variations of MSLP at a specific geographic point. On the other hand, as mentioned in Section 4.5, effective atmospheric perturbations in the GoO usually last less than 12 h. Therefore, any powerful changes within a period of less than 12 h at a specific geographic point may be considered a potential driving force in this region. To address this issue, it is necessary to look at the atmospheric conditions within the months of interest.
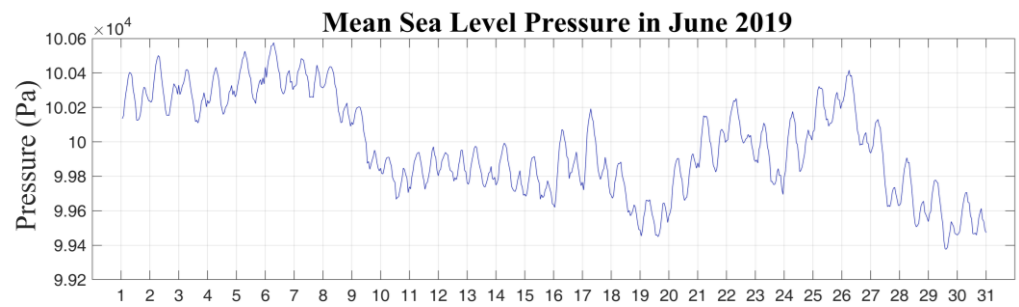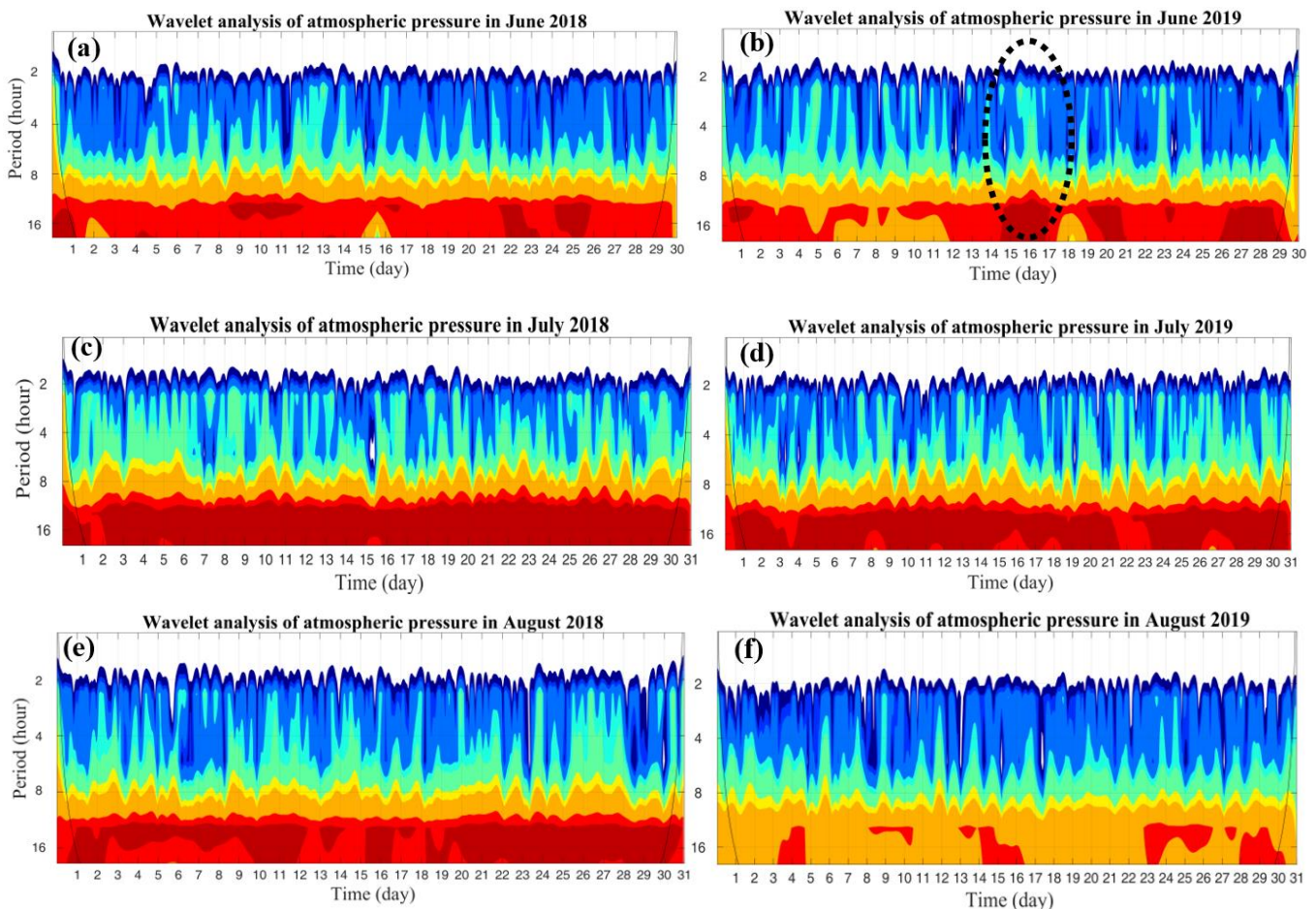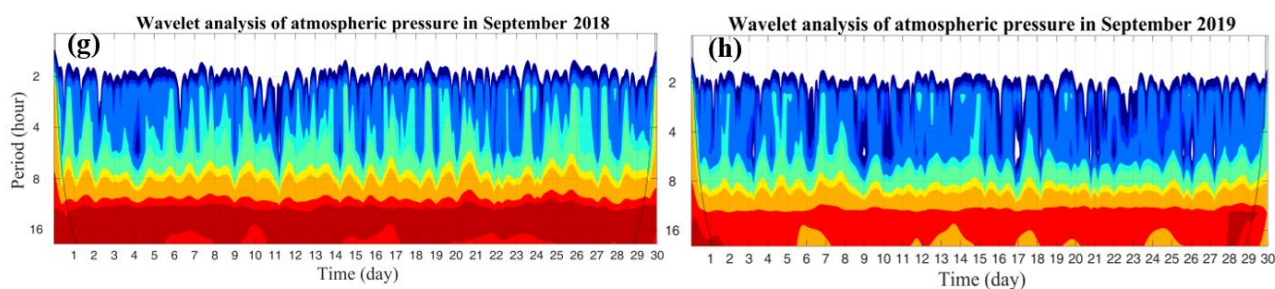
**Figure 20.** ERA5 mean sea level atmospheric pressure variation at the point P shown in Figure 1.

To study the MSLP oscillations at point P, wavelet analysis was applied to the MSLP time series at this point in 2018 and 2019 for each month separately, using a wavelet software provided by Torrence and Compo [50] (available online: http://atoc.colorado.edu/research/wavelets/, accessed on 12 September 2021) Figure 21 illustrates the wavelet power spectrum of MSLP from June to September in 2018 and 2019. The number of oscillations with a period less than 8 h reaches its maximum in June and, moreover, despite the difference in 2018 and 2019, there is no noticeable total difference between June, August, and September. It shows that the possible exciting forces are not less active during summer than in June. As an example, the power increment corresponding to the packet P3 in TerraSAR-X image analyzed in the previous section has been marked with a dashed ellipse in Figure 21b (see Section 4.5).

**Figure 21.** Wavelet spectrum of mean sea level atmospheric pressure at point P from June to September in 2018 and 2019; the dashed ellipse in (**b**) shows a surge in the power spectrum in periods less than 12 h on 28 September 2018, corresponding to the packet P3 in TerraSAR-X image analyzed in the previous section (See Section 4.5).

It is also necessary to evaluate the violation of the Brag threshold in this period. To do this, each month's data in 2018 and 2019 were combined and, afterward, the ratios were calculated for the combined data. Figure 22 illustrates the ratio of ERA5 winds with a speed higher than 3 m/s, as the Brag threshold, in the GoO from June to September in combined 2018 and 2019. From a probabilistic view, the higher this ratio is, the less probability there is for ISW to be observed in that month. The results demonstrate that the ratios are the least in June and highest in July and August. Moreover, the pattern of the spatial distribution of the ratios shows that there is generally less possibility of observing ISWs in satellite images in the northern part than in the southern part of the GoO.
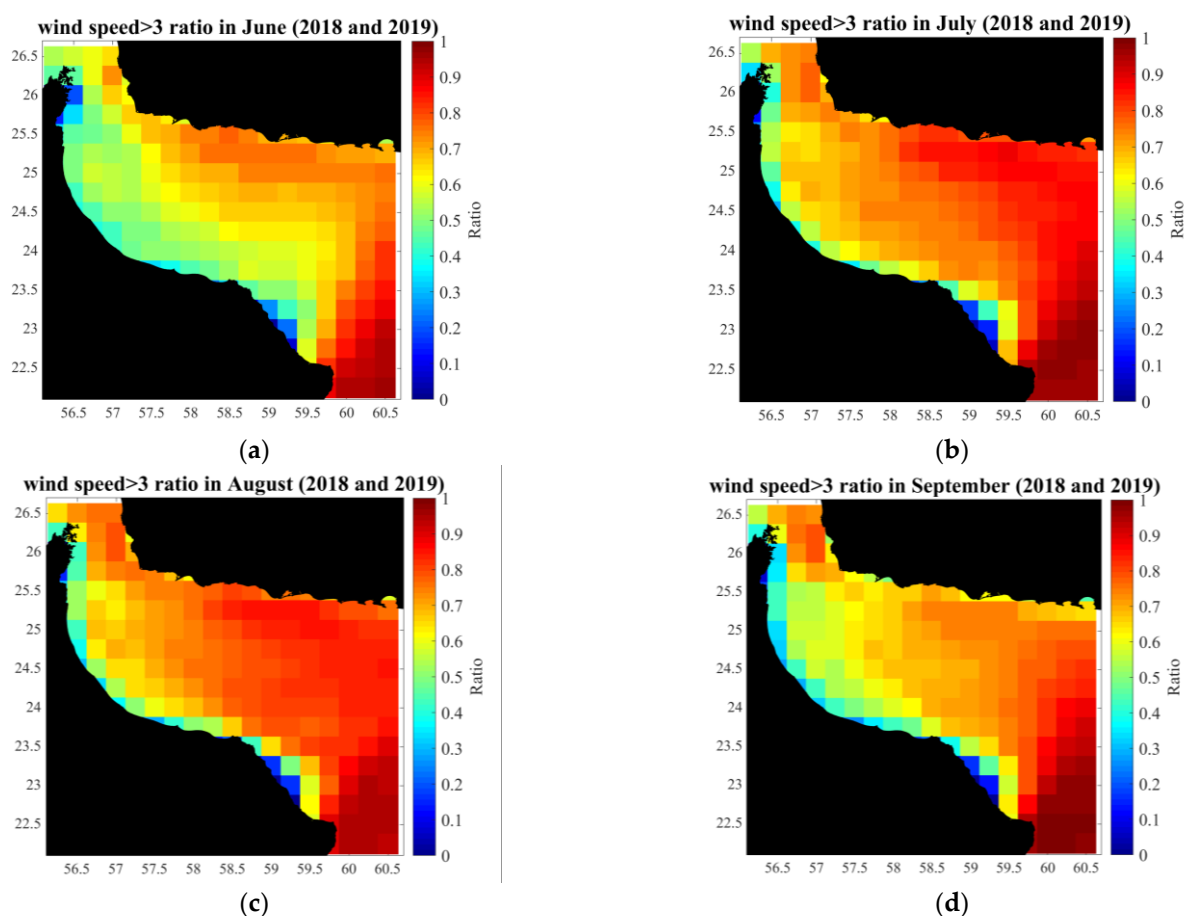


**Figure 22.** The ratio of the times when the wind speed was higher than 3 m/s in ERA5 data in (**a**) June, (**b**) July, (**c**) August, and (**d**) September in 2018 and 2019. The data for each month in 2018 and 2019 were combined and then the ratios were calculated.

According to these results, it is deducible that, first, there are most probably more waves than detected using satellite images in summer (July to September) but not detected due to blowing winds with speeds higher than the Brag threshold at the time of capturing. Second, zones 2 and 6 (the northern and eastern parts of the GoO) may be more active than identified in the previous section and further data from other sources such as field observations is essential to evaluate the characteristics of ISWs in these regions.

## 5. Conclusions

In this paper, we have presented the analysis for an ensemble of internal solitary waves observed in the SAR satellite images for almost a three-year period 2018–2020 in the Gulf of Oman. First of all, we described the variation of stratification in the GoO and demonstrated that it is well-pronounced in the summer season and almost disappears in the winter season. In the summer, the stratifedation can be approximated by a two-layer model with the pycnocline located at a depth of 25–30 m below the surface. Using the WOA profiles, we evaluated the spatiotemporal variations of coefficients of the JKKD equation in the GoO, including speeds of linear internal waves, and nonlinear and dispersion coefficients. Moreover, two model equations describing long internal waves in the shallow region (the KdV equation) and deep regions (the BO equation) were introduced for two states of stratification in the GoO.

All the observed ISWs were categorized by the possible generation mechanisms, depth of their appearance, and specific zones in the GoO where they basically emerge. Moreover, different potential mechanisms of generation were evaluated in the GoO including tides, flows around the underwater sill, atmospheric perturbations (pressure and wind fields), eddies, and Kelvin-type surges. Additionally, a zonation map of the GoO was suggested showing different characteristics of ISWs including number of incidence, possible mechanisms, and directions of propagation in each zone.

All these data allow one to estimate the time of the year and zones in the GoO where the dynamics of internal waves are the most intense. Knowledge of this information can be used to not only evaluate the contribution of ISWs to mixing in the GoO but reduce the risk of the negative impact of ISWs on offshore engineering constructions (gas and oil platforms, underwater pipelines, etc.), coastal activity, as well as marine and submarine navigation. In perspective, a more detailed study of internal waves in the GoO can be undertaken using a combination of field instrumental measurement, satellite and aircraft images, as well as theoretical and numerical models.

# References

1. Alpers, W.; Wang-Chen, H.; Hock, L. Observation of Internal Waves in the Andaman Sea by ERS SAR. IGARSS 97. *Remote Sens. Sci. Vis. Sustain. Dev*. **1997**, *4*, 1518–1520. http://dx.doi.org/10.1175/JPO-D-16-0141.1.

2. Mitnik, L., Alpers, W., Lim, H. Thermal plumes and internal solitary waves generated in the Lombok Strait studied by ERS SAR. In *ERS-Envisat Symposium: Looking down to Earth in the New Millennium*, Gothenburg, Sweden, 16–20 October 2000.

3. Lavrova, O.; Mityagina, M. Satellite Survey of Internal Waves in the Black and Caspian Seas. *Remote Sens*. **2017**, *9*, 892. https://doi.org/10.3390/rs9090892.

4. Da Silva, J.C.; Magalhães, J.M.; Gerkema, T.; Maas, L.R. Internal solitary waves in the Red Sea: An unfolding mystery. *Oceanography* **2012**, *25*, 96–107. https://doi.org/10.5670/oceanog.2012.45.

5. Guo, C.; Vlasenko, V.; Alpers, W.; Stashchuk, N.; Chen, X. Evidence of short internal waves trailing strong internal solitary waves in the northern South China Sea from synthetic aperture radar observations. *Remote Sens. Environ*. **2012**, *124*, 542–550. https://dx.doi.org/10.1016/j.rse.2012.06.001.

6. Zhao, Z.; Liu, B.; Li, X. Internal solitary waves in the China seas observed using remote-sensing techniques: A review and perspectives. *Int. J. Remote Sens*. **2014**, *35*, 3926–3946. https://dx.doi.org/10.1080/01431161.2014.916442.

7. Lavrova, O.; Mityagina, M.; Sabinin, K.; Serebryany, A. Satellite observations of surface manifestations of internal waves in the Caspian Sea. *Izv. Atmos. Ocean. Phys*. **2011**, *47*, 1119–1126. https://doi.org/10.1134/S000143381109009X.

8. Gao, Q.; Dong, D.; Yang, X., Husi, L., Shang, H. Himawari-8 Geostationary satellite observation of the internal solitary waves in South China Sea. In Proceedings of the 2018 ISPRS TC III Mid-term Symposium "Developments, Technologies and Applications in Remote Sensing", Beijing, China, 7–10 May 2018; pp. 363–370. https://doi.org/10.5194/isprs-archives-XLII-3-363-2018.

9. Magalhaes, J.M.; Da Silva, J.C.B. Internal Solitary Waves in the Andaman Sea: New Insights from SAR Imagery. *Remote Sens*. **2018**, *10*, 861. https://doi.org/10.3390/rs10060861.

10. Hesari, A.R.E.; Andi, S.; Farjami, H. Study of internal waves in the Persian Gulf using field data and satellite images. *Int. J. Coast. Offshore Eng*. **2019**, *2*, 9–16.

11. Karang, I.; Chonnaniyah, N.; Osawa, T. Internal solitary wave observations in the Flores Sea using the Himawari-8 geostationary satellite. *Int. J. Remote Sens*. **2019**, *41*, 5726–5742. https://doi.org/10.1080/01431161.2019.1693079.

12. Small, J.; Martin, J. The generation of non-linear internal waves in the Gulf of Oman. *Cont. Shelf Res*. **2002**, *22*, 1153–1182.

13. Jackson, C.R.; Apel, J.R. *An Atlas of Internal Solitary-like Waves and Their Properties*, 2nd ed.; Global Ocean Associates: Rockville, MD, USA, 2004. Available online: http://www.internalwaveatlas.com/Atlas2_index.html (accessed on 22 October 2020).

14. Massel, S.R. *Internal Gravity Waves in the Shallow Seas*; Springer International Publishing: Berlin/Heidelberg, Germany, 2015.

15. Leonov, A.I.; Miropolsky, Y.Z. Resonant excitation of internal gravity waves in the ocean by atmospheric pressure fluctuations. *Izv. Acad. Sci. USSR Ser. Atmos. Ocean. Phys*. **1973**, *9*, 480–485.

16. Morozov, E.G. *Oceanic Internal Tides: Observations, Analysis and Modeling*; Springer International Publishing: Berlin/Heidelberg, Germany, 2018.

17. Benilov, A.Y.; Solntseva, N.I.; Filyushkin, B.N. Relationship between the variability of the wind field and internal waves. *Oceanolog* **1978**, *18*, 257–266.

18. LeBlond, P.H., Mysak, L.A. *Waves in the Ocean*; Elsevier Oceanography Series; Elsevier: Amsterdam, The Netherlands, 1978; Volume 20.

19. Fu, L.L.; Holt, B. Some examples of detection of oceanic mesoscale eddies by the SEASAT synthetic-aperture radar. *J. Geophys. Res. Oceans* **1983**, *88*, 1844–1852. https://dx.doi.org/10.1029/JC088iC03p01844.

20. Joyce, T.M.; Stalcup, M.C. An upper ocean current jet and internal waves in a Gulf Stream warm core ring. *J. Geophys. Res. Oceans* **1984**, *89*, 1997–2003.

21. Lyzenga, D.; Wackerman, C. Detection and classification of ocean eddies using ERS-1 and aircraft SAR images. *Variations* **1997**, *414*, 1267.

22. Sandven, S.; Johannessen, O.M. High-frequency internal wave observations in the marginal ice zone. *J. Geophys. Res*. **1987**, *92*, 6911–6920.

23. Johannessen, O.M.; Sandven, S.; Chunchuzov, I.P.; Shuchman, R.A. Observations of internal waves generated by an anticyclonic eddy: A case study in the ice edge region of the Greenland Sea. *Tellus A Dyn. Meteorol. Oceanogr*. **2019**, *71*, 1652881.

24. Morvan, M.; Carton, X.; Corréard, S.; Baraille, R. Submesoscale dynamics in the Gulf of Aden and the Gulf of Oman. *Fluids* **2020**, *5*, 146. https://doi.org/10.3390/fluids5030146.

25. Koohestani, K.; Allahdadi, M.N.; Chaichitehrani, N. Oceanic Response to Tropical Cyclone Gonu (2007) in the Gulf of Oman and the Northern Arabian Sea: Estimating Depth of the Mixed Layer Using Satellite SST and Climatological Data. *J. Marine Sci. Eng*. **2021**, *9*, 1244. https://doi.org/10.3390/jmse9111244.

26. Hogg, A.M.; Dewar, W.K.; Berloff, P.; Ward, M.L. Kelvin wave hydraulic control induced by interactions between vortices and topography. *J. Fluid Mech*. **2011**, *687*, 194–208.

27. Khalilabadi, M.R.; Aliakbari Bidokhti, A.A.; Nazarian, M. Long waves generated by storms in the Gulf of Oman. In Proceedings of the 8th Conference of Fluid Dynamics, Tabriz, Iran, 8 September 2003

28. Koohestani, K., Allahdadi, M.N., Kamalian, U.R. Observed response to cyclone Ashobaa along coasts of Arabian Sea and Gulf of Oman. *Am. J. Fluid Dyn*. **2018**, *8*, 19–29.

29. Ranji, Z.; Soltanpour, M. On the effects of Cyclone Ashobaa on sub-inertial oscillations over the Arabian Sea. *Cont. Shelf Res*. **2021**, *222*, 104435.

30. Thrope, S.A. The excitation, dissipation, and interaction of internal waves in the deep ocean. *J. Geophys. Res*. **1975**, *80*, 328–338. https://doi.org/10.1029/JC080i003p00328.

31. Chaichitehrani, N.; Allahdadi, M.N. Overview of Wind Climatology for the Gulf of Oman and the Northern Arabian Sea. *Am. J. Fluid Dyn*. **2018**, *8*, 1–9.

32. Locarnini, R.; Mishonov, A.; Baranova, O.; Boyer, T.; Zweng, M.; Garcia, H.; Reagan, J.; Seidov, D.; Weathers, K.; Paver, C.; et al. *World Ocean Atlas 2018*; U.S. Department of Commerce: Washington, DC, USA, 2019; Volume 1: Temperature.

33. Copernicus Climate Change Service (C3S) (2017): ERA5: Fifth Generation of ECMWF Atmospheric Reanalyses of the Global Climate. Copernicus Climate Change Service Climate Data Store (CDS). Available online: https://cds.climate.copernicus.eu/cdsapp#!/home (accessed on 16 November 2020).

34. Apel, J.R.; Ostrovsky, L.A.; Stepanyants, Y.A.; Lynch, J.F. Internal solitons in the ocean and their effect on underwater sound. *J. Acoust. Soc. Am*. **2007**, *121*, 695–722. https://dx.doi.org/10.1121/1.2395914.

35. Klein, C.; Saut, J.-C. *Nonlinear Dispersive Equations*; Springer, New York, NY, USA, 2021.

36. Khalilabadi, M.R.; Sadrinassab, M.; Chegini, V.; Akbarinassab, M. Internal wave generation in the Gulf of Oman (outflow of Persian Gulf). *Ind. J. GeoMarine Sci*. **2015**, *44*, 371–375.

37. Khan, S.; Yang, S.; Bingchen, X.; Bradley, D.; Ahmed, N.; Shengchun, P. Subsurface highly saline water variability in the Gulf of Oman. In Proceedings of the OCEANS 2019-Marseille, Marseille, France, 17–20 June 2019; pp. 1–4.

38. Bidokhti, A.A.; Ezam, M. The structure of the Persian Gulf outflow subjected to density variations. *Ocean Sci*. **2009**, *5*, 1–12.

39. Khalilabadi, M.R.; Sadrinasab, M.; Chegini, V.; Akbarinasab, M. Three dimensional modeling of nonlinear internal waves in the Gulf of Oman shelf region. *J. Oceanog*. **2015**, *6*, 19–28.

40. Khalilabadi, M.R. A numerical study of internal tide generation due to interaction of barotropic tide with bottom topography in the Oman Gulf. *J. Earth Space Phys*. **2016**, *42*, 645–656. https://dx.doi.org/10.22059/jesphys.2016.57903.

41. Ablowitz, M.J.; Baldwin, D.E. Nonlinear shallow ocean-wave soliton interactions on flat beaches. *Phys. Rev. E* **2012**, *86*, 036305. https://dx.doi.org/10.1103/PhysRevE.86.036305.

42. Ostrovsky, L.A.; Stepanyants, Y.A. Kinematics of interacting solitons in two-dimensional space. *Russ. J. Earth Sci*. 2020, 20, ES4007. https://dx.doi.org/10.2205/2020ES000735.

43. Stepanyants, Y. The Asymptotic Approach to the Description of Two-Dimensional Symmetric Soliton Patterns. *Symmetry* **2020**, *12*, 1586. https://doi.org/10.3390/sym12101586.

44. Jackson, C.R.; da Silva, J.C.B.; Jeans, G.; Alpers, W.; Caruso, M.J. Nonlinear Internal Waves in Synthetic Aperture Radar Imagery. *Oceanography* **2013**, *26*, 68–79. https://dx.doi.org/10.5670/oceanog.2013.32.

45. Copernicus Marine Service (CMEMS). Global Ocean Physics Reanalysis (GLORYS12V1). Available online: https://resources.marine.copernicus.eu/product-detail/GLOBAL_MULTIYEAR_PHY_001_030/INFORMATION (accessed on 4 May 2021).

46. Robinson, I.S. Internal waves. In *Discovering the Ocean from Space*; Springer Praxis Books; Springer: Berlin/Heidelberg, Germany, 2010; pp. 453–483. https://doi.org/10.1007/978-3-540-68322-3_12.

47. Da Silva, J.C.B.; Ermakov, S.A.; Robinson, I.S.; Jeans, D.R.G.; Kijashko, S.V. Role of surface films in ERS SAR signatures of internal waves on the shelf: 1. Short-period internal waves. *J. Geophys. Res*. **1998**, *103*, 8009–8031. https://dx.doi.org/10.1029/97JC02725.

48. Zhao, Z.; Klemas, V.; Zheng, Q.; Li, X.; Yan, X.-H. Estimating parameters of a two-layer stratified ocean from polarity conversion of internal solitary waves observed in satellite SAR images. *Remote Sens. Environ*. **2004**, *92*, 276–287.

49. Da Silva, J.C.B.; Ermakov, S.A.; Robinson, I.S. Role of surface films in ERS SAR signatures of internal waves on the shelf, 3. Mode transitions. *J. Geophys. Res*. **2000**, *105*, 24089–24104. https://dx.doi.org/10.1029/2000JC900053.

50. Torrence, C.; Compo, G.P. A practical guide to wavelet analysis. *Bull. Amer. Meteor. Soc*. **1998**, *79*, 61–78.